



HAL
open science

Automated method for real-time AMD screening of fundus images dedicated for mobile devices

Sofien Ben Sayadia, Yaroub Elloumi, Rostom Kachouri, Mohamed Akil, Asma Ben Abdallah, Mohamed Hedi Bedoui

► **To cite this version:**

Sofien Ben Sayadia, Yaroub Elloumi, Rostom Kachouri, Mohamed Akil, Asma Ben Abdallah, et al.. Automated method for real-time AMD screening of fundus images dedicated for mobile devices. Medical and Biological Engineering and Computing, 2022, 10.1007/s11517-022-02546-8 . hal-03621710

HAL Id: hal-03621710

<https://hal.science/hal-03621710v1>

Submitted on 28 Mar 2022

HAL is a multi-disciplinary open access archive for the deposit and dissemination of scientific research documents, whether they are published or not. The documents may come from teaching and research institutions in France or abroad, or from public or private research centers.

L'archive ouverte pluridisciplinaire **HAL**, est destinée au dépôt et à la diffusion de documents scientifiques de niveau recherche, publiés ou non, émanant des établissements d'enseignement et de recherche français ou étrangers, des laboratoires publics ou privés.

Automated Method for Real-Time AMD Screening of Fundus Images Dedicated for Mobile Devices

Sofien BEN SAYADIA^{a,b,c}, Yaroub ELLOUMI^{a,b,c}, Rostom KACHOURI^b, Mohamed AKIL^b, Asma BEN ABDALLAH^a, Mohamed Hedi BEDOUI^a

Sofien BEN SAYADIA: sofien.bensayadia@esiee.fr

^aMedical Technology and Image Processing Laboratory, Faculty of medicine, University of Monastir, Tunisia.

^bLIGM, Univ Gustave Eiffel, CNRS, ESIEE Paris, F-77454 Marne-la-Vallée.

^cUniversité de Sousse, ISITCom, 4011, Hammam Sousse, Tunisie.

Abstract

Aged Macular Degeneration (AMD) leads to a progressive decline in visual acuity until reaching blindness. It is considered as an irreversible pathology where an early diagnosis remains crucial. However, the lack of ophthalmologists, the permanent increase in elderly people and their limited mobility involves a delay in AMD diagnosis.

In this paper, we propose an automated method for AMD screening. The proposed processing pipeline consists in applying the well-known radon transform to the macula region in order to model the AMD lesions even with a moderate quality of smartphone captured fundus images. Thereby, the relevant features are carefully selected, related to the main proprieties of drusens, and then provided to an SVM classifier. The implementation of the method into a smartphone associated to a fundus image capturing device leads to a mobile CAD system that performs higher performance AMD screening. Within this framework and, to achieve a real time implementation, an optimization approach is suggested in order to reduce the processing workload.

The evaluation of our method is carried out through the three public STARE, REFUGE and RFMID databases. A 4-fold cross validation approach is used to evaluate the method performance where accuracies of 100%, 95.2%, 94.3% are respectively obtained with STARE, REFUGE and RFMID databases. Comparisons with the state-of-the-art methods in the literature are done. Thereafter, the robustness of the proposed method was evaluated and proved. We note that 100% accuracy was preserved despite the use of degraded quality fundus images as noisy and blurred. Moreover, the propounded method was implemented in S7-Edge and S9 Smartphone devices, where the execution times of 19 and 15 milliseconds were respectively achieved, which proves the AMD real time detection.

Taking advantage of its mobility, cost-effective, detection performance and reduced execution time, our proposed method seems a good solution for real time AMD screening on mobile devices.

Keywords: Aged macular degeneration, fundus image, drusens, radon transform, feature extraction, real-time, m-health

1. Introduction

Aged Macular Degeneration (AMD) is a chronic irreversible pathology which leads to a gradual decline in visual acuity until reaching blindness. In healthy color fundus images, the macular region is usually described as a darker region, where darkness increases

This work was supported by the PHC-UTIQUE 19G1408 Research program.

towards the center of the macula due to increased pigmentation, as depicted in Fig. 1a. However, AMD causes appearing drusens in the macula, which correspond to yellowish-white spots located under the layer of pigmented epithelial cells in the retinal image, as shown in Fig. 1b. The AMD pathology stages are categorized based on the drusen diameter, which is between 15 μm and 63 μm in the early AMD stage, between 63 μm and 125 μm in the intermediate stage, and above 125 μm in the later stage [1, 2]. The World Health Organization reports that eight million people have severe blindness due to AMD. However, if diagnosed at an early stage, the risk of progression to a late stage of AMD can effectively be slowed down through an AMD dedicated therapy. Hence, an early diagnosis is of utmost importance.

A fundus image, which is captured by the fundus camera, is used to diagnose and detect retinal diseases. Evidently, the usual diagnosis approaches require qualified ophthalmologists to acquiring retinal images and diagnose AMD. However, a low rate of ophthalmologists worldwide is registered, which is equal to 29 per million persons [3]. This leads to considerable waiting time, hence the delay between the AMD disease on set and the first diagnosis. Furthermore, this limitation will be aggravated in future years. In fact, the AMD pathology frequency rises for elderly people over 55 years [3]. The central statistics office has shown that the older population is expected to increase more than threefold between 2016-2051 [4], where the number of patients is expected to grow to 288 million affected individuals in 2040 [5]. Contrariwise, the ophthalmologist rate will remain stationary. Besides, AMD patients have a limited mobility, which inhibits traveling for medical examination. In addition, the usual approaches are performed by expensive equipment, making the AMD diagnosis costly. Consequently, those limitations contribute to the increasing risk of AMD progression to a late stage [6, 7].

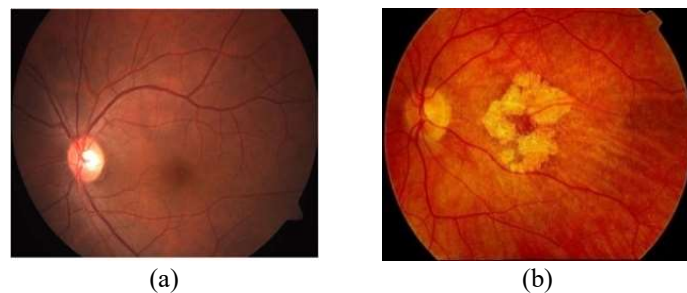


Fig.1 Symptoms of AMD: (a) Image of healthy retina; (b) Image of AMD-affected retina

Currently, smartphones present an excellent opportunity to improve the medical practice in several healthcare domains [8–11], particularly in ophthalmology. Several lenses are designed to be snapped onto smartphones in front of their cameras allowing capturing fundus images, as depicted Fig. 2. The lenses insure a Field Of View FOV between 45° and 50°, such as the Volk-N-View and Welch Allyn Panoptic Ophthalmoscope. These lenses have provided fundus images containing all retinal structures such as the blood vessel tree and the macula. Some clinical works are interested in studying the quality of Smartphone-Captured Fundus Images (SCFIs) [12], where the study proposed in [13] assigned that they were readable with an average of 86% to 100%. Other studies affirmed that SCFI are sufficiently readable to identify the AMD [14].

In this paper, the main objective of our work is to provide an automated method of AMD detection dedicated to mobile devices. The targeted method must ensure higher detection accuracy while respecting the timing constraint with respect to the clinical use. The proposed method is intended to be implemented on a smartphone associated to a capturing device, to provide a Computer-Aided-Diagnosis (CAD) system for AMD screening. This CAD significantly allows the reduction of the overload placed on of ophthalmologists as

this, can be exploitable by non-ophthalmologist medical practitioners. The handheld aspect of the suggested CAD permits to use the CAD system in a limited clinical context, and so overcome the mobility limitations of patients. In addition, the system benefits from the cost-effectiveness of mobile phones and capturing devices. Consequently, this system overcomes the main problems that have caused a delay on the AMD diagnosis.



Fig.2 Optical lenses for retinal capture : (a) Volk-N-View [15]; (b) Welch-Allyn lens [16]

The clinical use requires that the proposed system provide an accurate assessment of the AMD pathology. The diagnosis should avoid false negative detection, which leads to expect serious disease states and results in an impractical treatment. Thus, the first challenge is to perform higher accuracy AMD screening despite the difficulty of drusen detection. The clinical employment requires a handled technology to be adapted to the patient mobility, which will become an alternative to the immobile classical fundus camera, as for angiographs and retino graphs. Due the handled aspect of smartphones, a light leakage normally occurs, which will lead to a noise in fundus images. Moreover, the non-stationary angle of SCFIs causes a lack of brightness and a non-balanced contrast. As a second challenge, the suggested method should prove the robustness in detecting AMD despite of the low contrast and blurred quality of SCFIs. Besides, with respect to increasing elderly people, the aimed CAD system should be used in clinical mass screening, which requires detecting AMD in a short time delay. Thus, the third challenge is to perform automatic AMD screening in reduced time, while respecting the limited processing capacities of smartphones and the permanent increase in the retinal image size.

Several studies have put forward automated AMD screening methods [1, 2, 17], but most of them have failed to provide optimal accuracy. Even in an opposite case, higher accuracy of existing methods is achieved due to the higher quality images, which cannot be guaranteed for SCFIs. Furthermore, the existing methods are always characterized by a higher computing complexity, which outreaches the capacity of mobile devices. Consequently, they cannot achieve reduced execution time, and so are not suitable for the aimed mobile CAD for AMD early diagnosis using SCFIs. Accordingly, our work is aimed at proposing a novel automated method for AMD screening that ensures accurate and robust detection despite the moderate quality of SCFIs with low execution time.

The rest of the paper is organized as follows: Section 2 provides an overview of the recent related works. Section 3 describes the suggested method steps as well as preprocessing, feature extraction, Section 4 details the implementation of our method into a mobile CAD system for AMD screening. Section 5 describes the conducted experimentations where robustness and real time implementations are analyzed with respect to the state-of-the-art. The choice of SVM parameters and oversampling techniques are justified. We finally draw a conclusion in section 6.

2. Related work

The proposed automatic methods for the AMD diagnosis are varied in terms of processing principles, which can be partitioned into image processing based methods and Machine Learning (ML) based ones. Most of image processing based methods have focused on segmenting drusens as regards their color and intensity [4, 6, 7, 18]. However, those criteria are confused with other pathological lesions. As indicated in the survey of [5], the methods based on classical ML for AMD disease/no disease detection have been widely used and generally achieved higher performance AMD detection.

This category of methods involves three main stages. The first one is the pre-processing step which consists in improving the quality of images and locating the regions of interest. The second stage proceeds to extract AMD features. Some work reduces the feature vector based on accuracy and then provides it to a classifier in order to screen the AMD disease. In this stage, most known classification algorithms are used, such as Support Vector Machines (SVMs), Decision Trees (DT), K-Nearest-Neighbors (KNN) and Random Forests (RF). A summary of AMD screening methods in terms of accuracy, complexity and inference time is presented in Table 1.

In [19], the authors used mathematical morphology to highlight drusen areas and healthy macular regions. Subsequently, features called “Hu moments” were calculated from each pixel. Then, a feature selection method was used to evaluate the predictive capability of features and to choose the ones that were highly correlated to AMD detection. Thereafter, the extracted features were utilized by the SVM classifier for healthy and AMD distinction. In the work described in [20], the features of higher order spectra, entropy, fractal dimension and Gabor wavelet were extracted from fundus images. Then, they were ranked in order to select the optimal ones. Those features were transmitted for the training while using the SVM. In [1], the authors proceeded to convert the two-dimensional fundus image into one-dimensional signals. They performed the empirical mode decomposition of the signal to distinguish healthy from AMD classes. Then, the nonlinear features were extracted to characterize and classify healthy and AMD fundus images using the SVM classifier. In the study presented in [2], the local configuration coefficients and the pattern occurrence features were used to classify the fundus images into healthy and AMD fundus images. Thereafter, they used the SVM classifier.

The accuracy of the methods based on classical ML largely depends on the type and quality of feature sets. However, most methods extract the features from the entire fundus image that contains anatomical structures, such as pathological lesions, Optic Disc (OD) and blood vessels, which have similar shapes as drusens and so might lead to higher false positive detection. Moreover, the previous studies did not explore all AMD morphological properties and often proceeded to extract redundancy features to identify the same propriety. For example, the methods suggested in [2, 21] were based only on the variation in the intensity in the fundus image while the method proposed in [19] was based only on the drusen color. As a consequence, they would fail to achieve a higher accuracy in real patient visual outcomes.

In addition, method evaluations are always performed using database images containing retino graph captured images, with a higher quality compared to SCFI ones, as indicated in second column of Table 1. Even through the evaluation of several methods is applied on high quality images, some methods have failed to achieve optimal accuracy [2, 21], like the work proposed in [19] which had non optimal accuracy from 92% to 83.5%. Such performances have not been adequate for the aimed CAD system for AMD detection. It should be noticed that several fundus image databases have been employed for evaluation, such as ARIA and KMC, where Structured Analysis of Retina (STARE) has been the most

used. Since the detection performance has been the unique objective of such works, all methods have implemented on desktops through the MATLAB software tool.

Furthermore, the existing methods are always aimed to achieve higher accuracy, without focusing on the computational performance. It can be deduced from columns “complexity” of Table 1, that the methods involve higher computationally processing caused by the large number of extracted features. The works reported in [1, 2, 20, 22], [23] led to extract 1262, 1000, 2068, 22 and 50–400 features respectively. Added to that, several features required iterative and recursive processing. Some feature processing achieved a complexity of about $O(n^3)$ and $O(n^4)$, like the third order Higher Order Spectral (HOS), the bis-spectrum [24] and H-jorth processing [21], where $(n \times n)$ was the fundus image dimension. In addition, some works have remedied for feature selection methods to enhance the classification performance. The selection process consisted in comparing all combination subsets of features to identify the ones having a higher correlation with the ground truth. The time complexities of selection were in terms of evaluated combination subsets k , where it achieved a polynomial complexity of $O(n^{k+1})$ [25]. Both criteria deteriorated the time complexity of AMD screening methods [5]. Moreover, the rise in the image size resulted in a similar increase in the execution time. It is observed in Table 1, that although the methods are evaluated using high-performant architectures, the time needed for feature extraction and classification is in the order of 39 seconds - 2.5 hours, as indicated in column 4. The execution time will be aggravated when implemented in mobile devices due to the limited processing capacity. Therefore, the existent AMD detection methods are not suitable for mobile CAD systems of AMD screening.

Table 1 Accuracies and computational performances of AMD screening methods

Works	Data base	Accuracy	Execution time (s)	Complexity	Machine
(Mookiah et al., 2015a)[1]	ARIA	85.09%	9,496. 231	$O(n^3)$	Intel i7-4770, 3.47 GHz/16 GB Matlab 2012b
	STARE	100%			
	KMC	91.67%			
(Mookiah et al., 2015b)[2]	STARE	97.78%	109.550	$O(n^2)$	Intel i7-4770 3.47 GHz/16 GB Matlab 2012b
(Mookiah et al., 2014a)[20]	ARIA	95.07%	39.017	$O(n^3)$	Intel i7-4770 3.47 GHz/16 GB Matlab 2012b
	STARE	95.00%			
	KMC	90.19%			
(Mookiah et al., 2014b)[22]	KMC	93.70%	87.78	$O(n^2)$	Intel i7-4770 3.47 GHz/16 GB and MATLAB 2012b
(Acharya et al., 2017)[21]	KMC	85.12%	NA	$O(n^4)$	MATLAB
(Acharya et al., 2016)[17]	ARIA	96.89%	NA	$O(n^2)$	MATLAB
	STARE	100.00%			
	KMC	99.49%			

The contribution of our work is to suggest a new automated method for detecting the AMD disease dedicated to mobile devices, which will ensures an accurate AMD detection with respect to the state of the art screening techniques. Within this framework, our work aims to guarantee the robustness despite the low quality of SCFIs in addition to assuring AMD detection in real execution time even with the limited capacity of smartphones.

3. AMD screening Method

Our work mainly focuses on the development of a new method dedicated to the mobile architecture to ensure a CAD for AMD screening with a higher detection performance and optimized processing time. The first step consists in pre-processing the fundus image to locate the macula and extract it as a Region Of Interest (ROI) in order to reduce false positive detection. Then, contrast enhancement is subjected to improve the fundus image quality, as described respectively in sub-section 3.1.1 and sub-section 3.1.2. Secondly, our contribution consists in modeling the AMD proprieties. For this purpose, the Radon Transform (RT) was applied to the macula region, which offers an explicit intensity representation and robustness with respect to the degraded image quality and with a minimal computational requirement, as detailed in the sub-section 3.2. Thereby, the method consists in adequately selecting the AMD features for image classification. Those features are selected to reflect all AMD proprieties modeled in the radon transform representation in order to ensure higher accuracy. Besides, it is proceeded to identify few features with lower complexities with respect to the limited capacity of smartphone architectures, as indicated in the sub-section 3.3. Those features are provided to a classifier which is chosen to assure higher performance AMD detection in a low execution time, as depicted in the sub-section 3.4, where the whole flowchart of the proposed method is presented in Fig. 3.

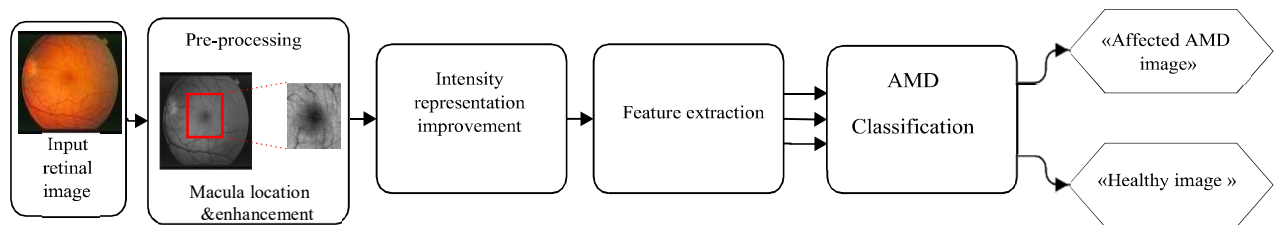


Fig.3 Flowchart of proposed method for AMD screening

3.1 Preprocessing

3.1.1 Macula ROI extraction

The AMD pathology leads the drusens to appear inside the macula[26]. Thus, exploring the macula region is sufficient to detect AMD, avoiding the need to explore the entire retina[27]. In addition, a whole retina analysis involves higher computational processing due to the permanent increase in the image size.

For that, we aim to locate the macula as a ROI. In fact, several approaches of macula detection have been suggested in the literature where the majority allowed effective detection. The work described in [28] used morphological operations followed by thresholding for segmenting the blood vessels and the darkest region property in fundus images. The suggested method provided 96% accuracy when tested on 100 images from the DRIVE and the STARE datasets. In [29], the macula was detected as a region in the retina having a low pixel intensity. However, the evaluation was performed without using AMD fundus images. The work proposed in [30]permitted locating the fovea, where a detection rate of 96.4% was achieved. However, their method was not evaluated with fundus images having a degraded quality. In [31],the method was able to detect the macula even in the presence of pathological lesions, which achieved higher accuracy equal to 96.6%. This method was characterized by a low complexity making it benchmarked using images with a size of 2304×1536 and locating the macula in 0.007 second. As a result, the method of [31]was is employed in our work to locate the macula while respecting the complexity constraint.

3.1.2 Contrast enhancement

The green channel is more informative and has a better contrast than red and blue channels [32, 33]. It explicitly represents the retinal shapes that are characterized by high intensity. For that, the green channel is extracted, which is in accordance with several AMD screening methods [1, 2, 17, 19, 20]. Thereafter, the drusens are mainly characterized by their higher intensity compared with their background. The drusens can be located with a higher performance if they belong to a homogeneous background. However, the ganglion cell layer is thinned continuously while going towards the fovea, which involves a steady decrease in intensity, as illustrated in Fig. 4a. Consequently, the regions containing drusens are characterized by a different contrast in relation to the distance from the fovea, where the regions close to the fovea are characterized by a higher contrast, while the regions around the macula have a reduced contrast. Furthermore, the smartphone capture brings to a non-stationary projection angle. Therefore, it involves a light leakage that causes an increasing contrast in partial region of the fundus image, as shown in Fig. 4b. As a result, the macula texture in smartphone capture leads to an unbalanced contrast with respect to the macula and the drusen lesions.

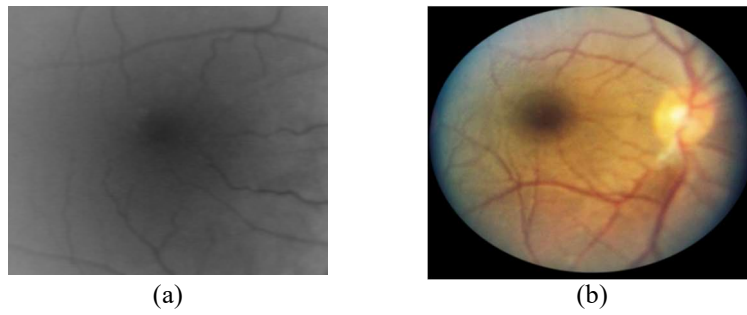


Fig.4 Illustration of unbalanced contrast caused by (a) macula texture (b) Smartphone captured fundus image

Classical Histogram Equalization (HE) consists in globally improving the contrast, through transforming the histogram of the whole image with a uniform range. Since the contrast and intensity distributions change from one region to another, HE is inadequate to rectify the unbalanced contrast problem [34]. To avoid this problem, the authors in [32] showed that some works of image enhancement technique had used the Contrast Limited Adaptive Histogram Equalization (CLAHE) algorithm which would divide the input image into non-overlapping regions and perform adaptive HE to each region separately. The pixel intensities were rectified with respect to their rank on the intensity histogram [32] of the sub-image. Consequently, the contrast was improved in each region even if they had unbalanced ones. In addition, the CLAHE method was performed on all pixels in the entire image where the computational complexity was equal to $O(n^2)$ [35], which was appropriate for targeting a timing-constrained implementation. Accordingly, the CLAHE algorithm was employed in our study to avoid the unbalanced contrast problem of fundus images.

3.2 Radon transform

A drusen is distinguished by its greater intensity in the macula sub-image [36], which serves as an important pathological feature to evaluate AMD risk. For this purpose, we represent the contrast variation in the macula image to highlight the intensity of drusens from their background. A very relevant example is the work proposed by [37], which consisted in applying the well-known RT [38] processing in order to represent the intensity of the Optic Disc (OD). The writers in [39] suggested a method for detecting retinal vasculatures based on the RT representation of the vessel brightness in fluorescein

angiography fundus images. Compared to other approaches, the RT improves low frequency components and can derive a large number of features [40]. The RT also improves the intensity of small drusens. It reflects information about the entire image texture rather than each pixel separately. Furthermore, it generates the radon values that are computed in terms of pixel sum, as illustrated with arrows in Fig. 5. Hence, the RT is distinguished by its robustness with respect to noise, whether caused by the retinal shape texture or by the smartphone capturing process[41]. Moreover, the RT converts a 2D image into a 1D projection, where deducing drusens from the radon vector requires significantly lower computational time than deducing them from the whole image[42].

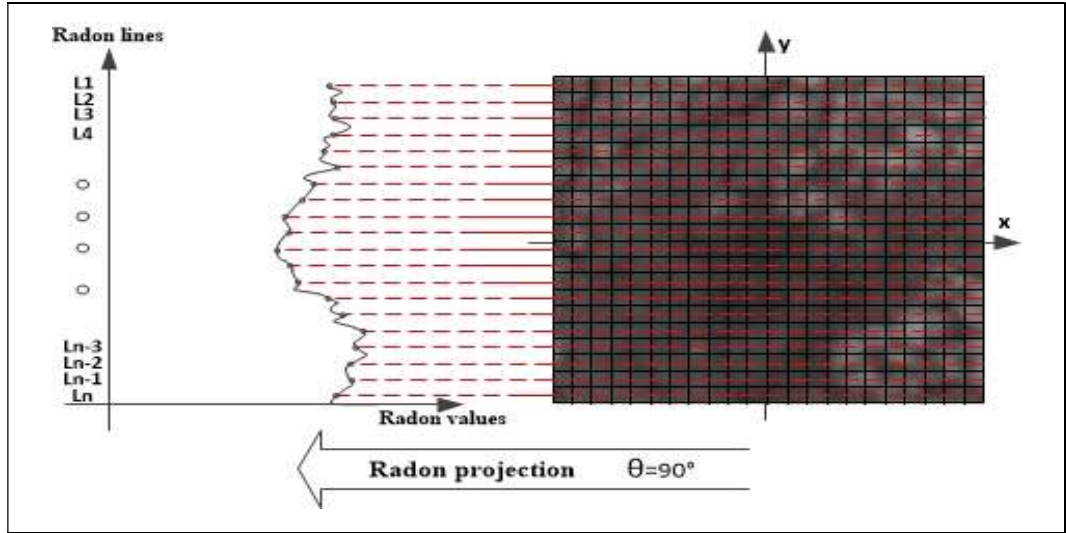


Fig. 5 Radon transform with angle 90°

The RT transforms the intensity of image pixels into line parameters, named the radon projection [20, 37]. The Radon transform R , for a two-dimensional image $I(x, y)$ maps an image to its integral on lines defined by angle θ and offset r , as formulated in Eq. (1)[43].

$$R(r, \theta) = \int \int_{-\infty}^{+\infty} I(x, y) \cdot \delta(x \cdot \cos(\theta) + y \cdot \sin(\theta) - r) dx dy \quad (1)$$

Where I is the input image, x and y are the pixel indices in I , r is the distance between the projection line and the image center, and θ is the angle between the projection line and the x -axis. δ is the dirac function, that integrates to 1 and has infinite value when evaluated at 0 and the value of 0 at all other points [44]. This allows for the summation of values along the line $x\cos(\theta)+y\sin(\theta)-r$ for a given θ and is equivalent to rotating an image θ degrees and integrating pixel intensities along the height of the rotated image.

As shown in the example Fig 5, when the image is passed through the RT, it were divided into several non-overlapping paths or beams per angle spaced at 1 pixel unit, as modeled as red dotted rows which are labelled from $L1$ to L_n . Assume that the image consists of M pixels in total, and that the intensity of the i th pixel is denoted by I_i , $i = 1, \dots, M$. The radon projection point value for each line would equal to the cumulative intensity of all M pixels. Each projection therefore contains the beam sums that are calculated at a given angle, as illustrated in Fig. 5, where the estimated radon projection of the macula image is given for angles equal to 90°.

The RT allows efficiency representing the intensity of an image in the radon domain as a collection of projections all along the different directions. In Fig. 6a, we illustrate the appearance of two drusens in a macula image, where the drusens and the macula are respectively simulated with light and dark colors. Thereafter, three radon projections are

applied to the sub-images with angles equal to 90° , 45° and 0° , in order to investigate the correlation between the radon projection angle and the drusen detection, as shown in Fig. 6.

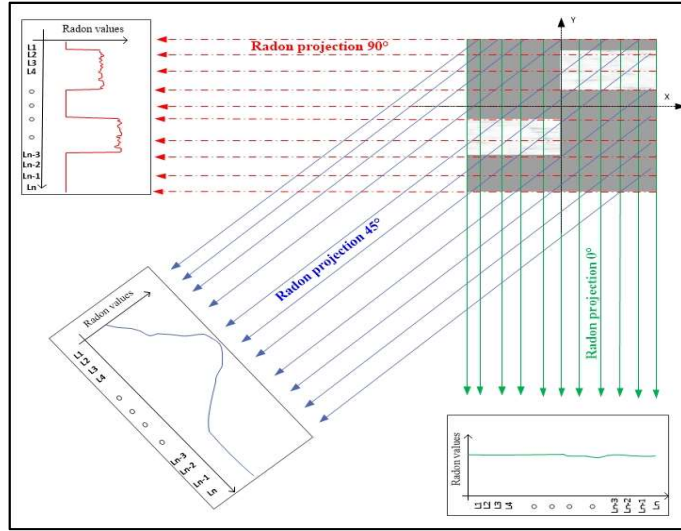


Fig. 6 Radon projection at angles 0° , 45° and 90° .

For the radon projection at the 90° angle, the drusen boundaries are defined as peaks in the radon vector. For the projection at the angle 45° , the drusens are aligned to the radon crossbars. Hence, the radon projection contains a large peak, which reflects the summation of the intensity of two drusens. This projection allows detecting the presence of drusens that can be obscured when presented separately. For the radon projection at angle 0° , the drusens appear as a large lesion with respect to the horizontal axis. They lead to a stationary value in the radon vector. Hence, the 0° projection fails to distinguish between the drusens and the background of macula.

In addition, we can see that both projections at 0° and 2° angles reflect radon vectors having stationary values. Thus, like the first projection 0° , projection 2° does not allow representing the drusen, as shown in Fig.7a. We can also see that the intensity variation is maintained even if we change the projection angle from 90° to 92° , where both illustrate the same drusen shapes, as depicted in Fig. 7b. At most angles that are too close together, the RT produces a similar projection, hence leading the higher excessive redundancy. Furthermore, a single radon projection involves covering all the macula image pixels with resolution $n \times n$, which requires $O(n^2)$ [45]. For that reason, the RT projection processing requires a complexity equal to $O(\omega \cdot n^2)$, where ω is the number of projections. Consequently, performing the RT in all directions of a circle requires a higher computational complexity of the generation of all radon projections[46].

In fact, we deduce that applying the RT with different projections provides complementary shape modeling of drusens. In order to achieve a reduced complexity, it is sufficient to apply the transformation only along a small set of different directions. At the same time, it is necessary to select angles while fixing the step values, in order to consider the distribution of drusens in various directions. Therefore, we investigate the correlation between the different numbers of radon projection and the AMD screening performances, as proceeded in related work [41, 47]. We experimentally derive the optimal number of radon projections, which provides maximal screening performance in reduced time, where the screening outcome is reported in the experimented results, indicated in sub-section 5.4.1. Then, all projections are concatenated and stored on a matrix called the radon space.

The radon space permits to model the global structure of the image not just a single pixel where a macula image and its correspondent radon space, as illustrated in Fig. 8.

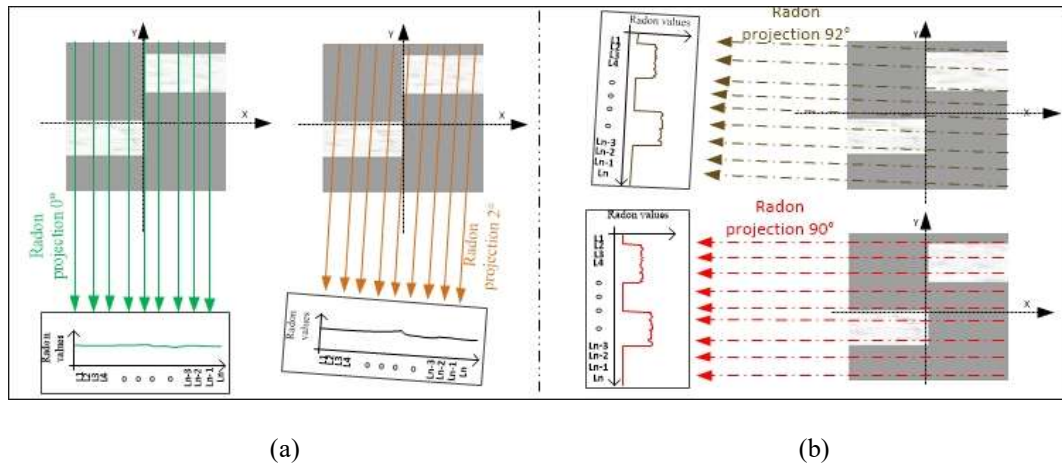


Fig. 7 Radon projection with close angles: (a) angles 0° and 2° ; (c) angles 90° and 92°

3.3 Proposed approach of feature extraction based upon Radon Transform

The radon space representations of the radon transformation are studied to identify the morphological properties of drusens in order to distinguish between healthy and AMD-affected macula images. Table 2 lists the different levels of AMD properties in terms of "irregularity distribution", "intensity growth" and "circular shape distortion" according to the AMD classification. In fact, retinal ganglia cells condense continuously, with the highest concentration in a radial direction towards the fovea, which involves a steady decrease in the intensity. As a result, a regular variation in the intensity is represented in the radon projection. However, a dispatched drusen in the macula image leads to the appearance of a greater irregular variation in the Radon projection [33], as depicted in the third column of Table 2, entitled "irregularity Distribution".

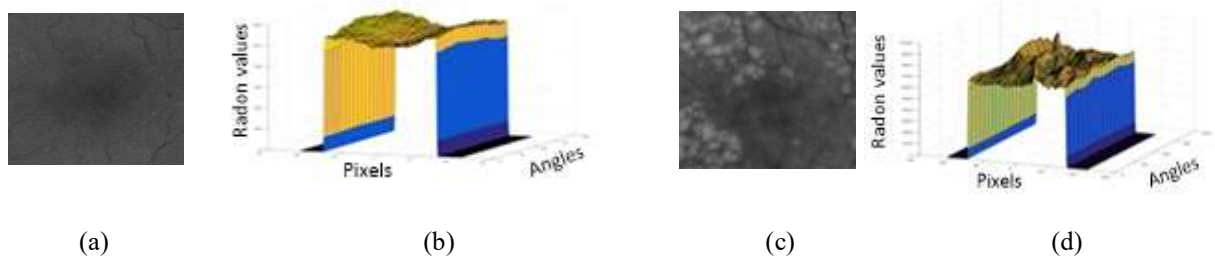


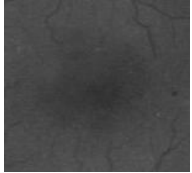
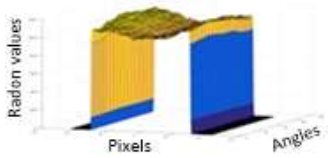
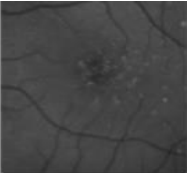
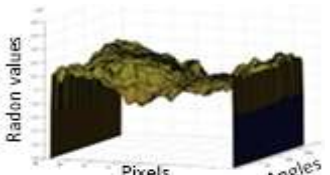
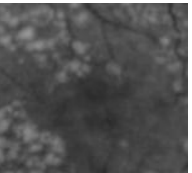
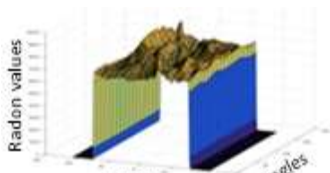
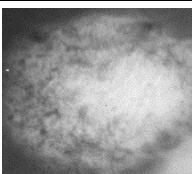
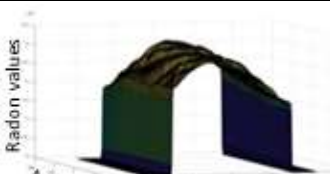
Fig.8 (a) Healthy macula; (b) Radon space of healthy macula ; (c) AMD affected macula; (d) Radon space of AMD affected macula

Furthermore, a healthy macula appears as a dark spot, where the fovea is the central part that provides the lowest pixel intensity compared to other regions. As a consequence, a radon projection has a downward slope followed by an upward one, with a main optimum in the macula center. However, drusens are characterized by a higher intensity compared to the other regions in the macula sub-image [48], which corresponds to a higher peak in the radon projection.

Due to the round shape of the macula and the centric position of the fovea [36], all radon projections have similar shapes [37, 49]. However, drusen presence destroys the circular formed shape of the macula, involving a valley in the radon projection. Since the radon projections are applied at different angles, the valley is expressed inside each radon

projection with a varied position, thus affecting the similarity between them. These three identified AMD properties can be used to distinguish AMD affected fundus images from healthy ones.

Table 2 AMD properties in terms of AMD grading

AMD grading		Radon space	Irregularity distribution	Intensity growth	Circular shape distortion
Healthy image			Low	Low	Low
AMD affected image	Early 		High	Low	Low
	Intermediate 		High	High	High
	Late 		Low	High	Low

Nevertheless, as shown in the second line of Table 2, we can see that the drusens in early stages are represented by low peaks that avoid their detection and do not alter the similarity between the radon projections. Drusens in the late stage also expand to coalesce and appear as large drusens, which implies the restoration of the regular distribution in the radon projection, as shown in the last row of the column “Irregularity distribution” of Table 2. Besides, the circular shape of the drusens in a late stage produces similar radon projections at different angles, as depicted in the last line of the column “Circular shape distortion” Table 2, leading to confusion between AMD images and healthy ones. A single individual property is not sufficient to detect drusens whatever the AMD stage is. To avoid those problems, the three identified properties should be combined, to complement each other and so produce the best distinction between healthy and AMD affected image.

Accordingly, we proceed to reflect each identified property with a single, robust and efficient feature. Those features are selected to reflect all AMD properties in order to ensure higher accuracy, as indicated in the following sub-sections. We focus on carrying out each feature processing with lower complexities in order to achieve a higher computational performance.

3.3.1 Irregularity distribution: Sample entropy

The texture of a healthy macula leads to a regular variation in the radon projection. The presence of drusens in the macula sub-image involves a higher irregular distribution in the

radon projection, with several optimal values. For that, we consider the radon projection variation to deduce AMD disease [1]. Usually, the entropy allows quantifying the signal regularity, such as the Kolmogorov–Sinai entropy [50], the approximate entropy [51], the Sample Entropy (SE) [52] and the spectral entropy [53]. In fact, the SE processing principle is based on computing a ratio between the number of successive values having the same direction and the number of successive values leading to inverting the direction [54]. The advantages of this entropy is the robustness to noise [55] and its independence of the signal length[56]. Therefore, the SE processing is chosen to deduce the radon projection irregularity.

The first step of the SE processing proceeds to identify a set S1 containing all sequences of consecutive points whether having growing or decreasing directions. Two Radon projections for a healthy and AMD affected macula are respectively shown in Fig. 9a and Fig. 9b, where the point sequences are modeled by boxes containing red and blue points. The second step consists in testing the following point of each sequence whether it follows a similar direction or not. For the direction conserved, the sequence is added to a set S2 of successive points. The following points of all sequences are represented by the green color, where sequences belonging to S2 are modeled by black boxes in both radon projections of Fig. 9. Then, a ratio between the sequence number in set S2 and set S1 is computed. Thereafter, the SE is computed by applying the natural logarithm of this ratio, as given in Eq. (2)[52, 57].

$$SE(m, r) = -\ln\left(\frac{S2(m+1,r)}{S1(m,r)}\right) \quad (2)$$

where m is the length of sequences, and r is the minimal difference to be considered when identifying the direction. With regard to optimal values for m and r , a developed tests of parameters for sample entropy [57] suggested that selecting m between 2 and 3 and r between 0.3 and 0.4 would give optimal classification results. Accordingly, in our work we proceeded to select m at 2 and r at 0.3 in order to have the optimal classification results.

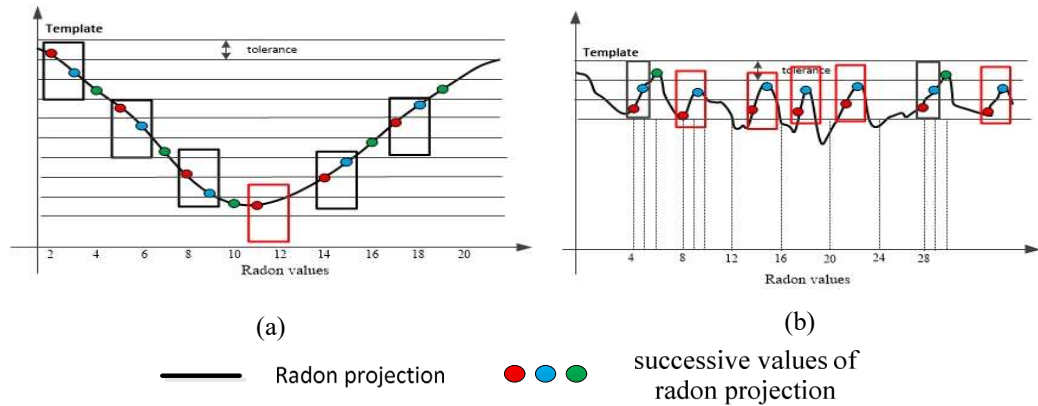


Fig.9 Radon projection with successive value location of : (a) Healthy macula, (b) AMD affected Macula

Therefore, a radon projection to a healthy macula has a regular variation with a single curvature in the middle of the radon vector. Hence, the sequence numbers in both S1 and S2 sets are very close, which are respectively equal to 6 and 5 in the case of Fig. 9a. Consequently, a healthy macula corresponds to a ratio near to 1, and so a SE value near zero. Contrary, a radon projection to an AMD affected macula has a higher variation, where the S2 set size is significantly smaller than S1 one. For Fig. 9b, S2 contains only two sequences, while S1 contains six, thus leading to a ratio close to 0. As a consequence, AMD affected macula results in a higher positive SE value.

As noted in sub-section 3.2, we deduced that modeling drusens in radon vectors depends on the projection angle. It can be seen that the stationary value of the radon projection at 0° does not allow modeling the intensity variation, which leads to a small SE value. In contrast, in case the projection angle is equal 90° , the radon vector contains ascending slopes followed by a descending one, which correspond to the intensity variation, hence the higher SE value. To avoid this problem, we computed the average Avg_{SE} of SE over different radon vectors with various angles, as indicated in Eq. (3).

$$Avg_{SE} = \frac{\sum_{\omega} SE(m,r)_{\omega}}{\omega} \quad (3)$$

where ω is the projection number. For an input RT vector having a size of $\sqrt{2} \times n$, the SE repeats the comparison over all possible sets, where the computational complexity is equal to $O(n^2)$ [58, 59]. Thus, while the SE is applied to all TR projections, the SE feature requires a complexity of $O(\omega \times n^2)$, and so leads to a higher computational complexity. To reduce the complexity, we aim to identify the minimal set of radon projections, which are selected to apply the SE that allows reducing execution time while expecting a maximal screening performance. Within this objective, we investigate the correlation between SE computing and the AMD screening performance, where the required set of radon projections is reported in the experimented section, indicated in the sub-section 5.4.

3.3.2 Intensity growth: dynamic threshold based intensity rate

Radon projection to a healthy image leads to provide a monotone signal. On the other hand, the radon projection of an AMD-affected image represents a higher peak that corresponds to the drusens. Accordingly, a threshold must be performed in order to efficiently separate needed peaks from background structures. In this way, many existing thresholding techniques [60], such as Otsu's local thresholding and the static threshold, can be chosen for this presented task. Nevertheless, we notice that Otsu's method does not provide an adequate threshold, if the number of peaks is small compared to the background or if the radon projection is severely corrupted by an additive noise [61, 62]. In addition, the uneven illumination used in the acquisition process results in different intensities for all captured fundus images, which leads to various values in the radon projection. Thus, a static threshold is not adequate to identify drusens based on their intensity peaks. For example, Fig. 10a and Fig. 10b correspond to the radon projection applied to dark macula sub-images, while Fig. 10c and Fig. 10d correspond to the radon projection applied to brightness ones. The static threshold modeled by red lines avoids the extraction of peaks. It extracts the value border of the radon projection as peaks in Fig. 10c, which leads to false positive screening of AMD. Moreover in Fig. 10d, the static threshold fails to extract peaks relative to drusen lesions due to the low values of the radon projection.

To avoid this problem, we apply a dynamic threshold based on the intensity rate for the radon space where level Th is identified with respect to the radon projection values, as modeled by green lines in Fig. 10. Thus, all the points of the radon projection having values greater than 0.9 times the difference between the maximal and minimal values are extracted, as depicted in Eq. 4.

$$Th = 0.9 * (\max R(i, j) - \min R(i, j)) \quad (4)$$

where Th is the threshold level, R is the radon space and (i, j) are the radon value indexes. We noted that the optimal threshold is adopted experimentally to 0.9, where the drusens having peaks greater than Th were examined, as proceeded in previous research [63]. This experimental approach allowed us to deduce that if such threshold is applied with a value below 0.9, some noise peaks or light leakage of the smartphone capture some noises has

been identified as lesions. In addition, we noticed that that if such a threshold applied with value greater than 0.9, some lesion were missed in the dark AMD affected macula.

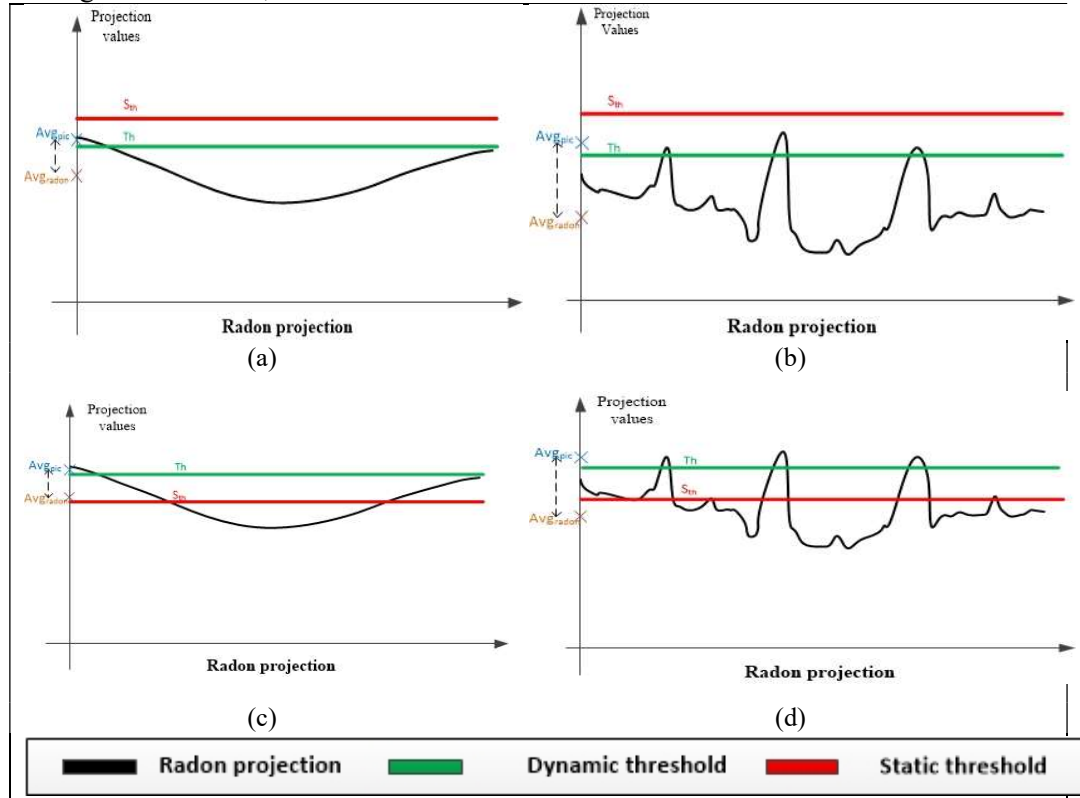


Fig. 10 Radon projections with static and dynamic threshold: (a) Dark healthy macula (b) Dark AMD affected macula, (c) Bright healthy macula (d) Bright AMD affected macula

Subsequently, we study the impact of the extracted values in the neighboring regions. Therefore, an average value of the radon projection avg_{radon} is computed, as given in Eq. (5). Then, we derive an average values of the extract peaks avg_{pic} , as provided in Eq. (6).

$$avg_{radon} = \frac{1}{w * p} \sum_1^w \sum_1^p R(i, j) \quad (5)$$

$$avg_{pic} = \frac{1}{n_{pic}} \sum_1^w \sum_1^p R(i, j) ; \text{ where } R(i, j) \geq Th \quad (6)$$

where w is the projection number, p is the radon projection size, and n_{pic} is the number of radon values $R(i, j) \geq Th$.

In fact, all values of the radon projection of a healthy macula are so close together that, the gap, between the maximal and minimal values, is small. Hence, avg_{pic} will be so close to the average of the radon projection avg_{radon} , as illustrated in Fig 10a and Fig. 10c. By way of contrast, for an affected macula representation, the values of the radon projection are so spaced, where the peaks relative to the drusens are characterized by higher values. Thus, a full appreciable gap between the avg_{pic} and avg_{radon} values is produced, as presented in Fig 9b and Fig. 10d. The idea is to deduce, the drusens presence based upon the image background, as proceeded in [63, 64]. To achieve this aim, we proceed to compute the ratio intensity growth feature $R_{intensity}$ between the average of peaks avg_{pic} and the average of the radon space avg_{radon} , as highlighted in Eq. (7)[64]

$$R_{intensity} = avg_{pic} / avg_{radon} \quad (7)$$

As a result, the ratio of the intensity growth feature $R_{intensity}$ of the healthy macula always tends towards 1. On the other hand, an AMD affected macula leads to a higher positive value of $R_{intensity}$. For the intensity growth feature, a threshold is applied to the

RT space projection with a size of $(\omega \times n)$. Then, a mean value of all peaks, within the entire RT space projection, is computed. Thus, it requires $O(\omega \times n)$ to be done.

3.3.3 Similarity: MSE

The radon projections to the healthy macula are characterized by a curvature shape formed by the degraded intensity variation, where the vertex of each radon projection corresponds to the fovea location[65]. Due to the round shape of the macula and the centric position of the fovea, all radon projections have a similar shape[37, 49], as illustrated in Fig. 11a. However, the radon projections of an AMD affected image involve the representation of valleys that are relative to drusens, and so distort the convex form. Since the drusens are located randomly in the macula region, and radon projections are applied with various angles, the valleys are expressed inside each radon projection with different positions as depicted in Fig. 11b. As a result, a big difference between radon vectors is distinguished.

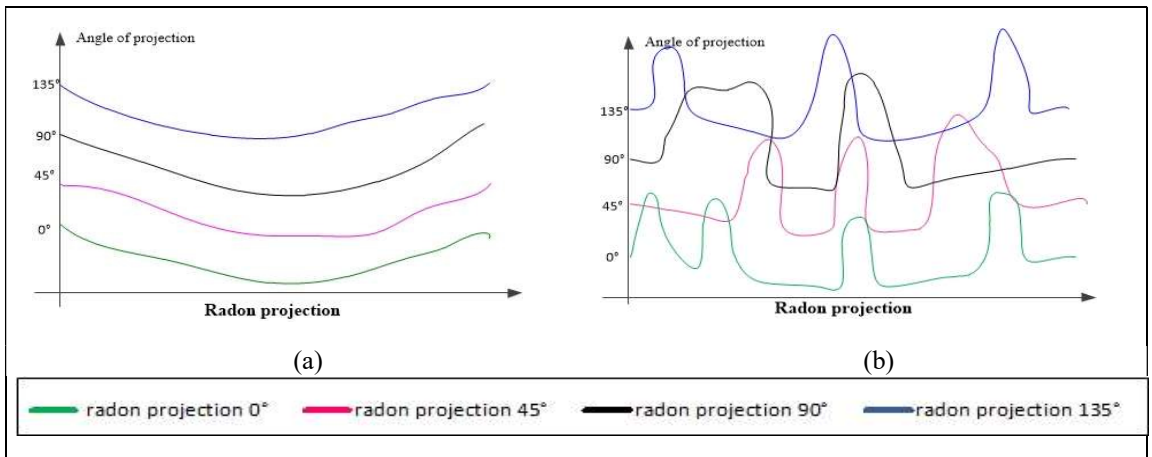


Fig. 11 Radon projection with 0° , 45° , 90° and 180° angles applied to: (a) Healthy macula; (b) AMD affected macula

Accordingly, we aim to quantify the difference between all radon projections to reflect the AMD disease. In fact, the measure of the dissimilarity between several models is attributed by the value of the distance from a universal model for all. For that, we compute the average vector $\bar{R}(N)$ of all projections, which is the average of the radon space $R_\omega(N)$ along all directions ω , as indicated in Eq (8).

$$\bar{R}(N) = \frac{1}{\omega} \sum_{\omega=1}^{\omega} R_\omega(N) \quad (8)$$

For a healthy macula, the average vector has a similar curvature to the original radon projections, as modeled by the red curvature in the radon projections at different angles, as represented in Fig. 12. Consequently, a minimal gap between the projections and the average projection curvature is provided.

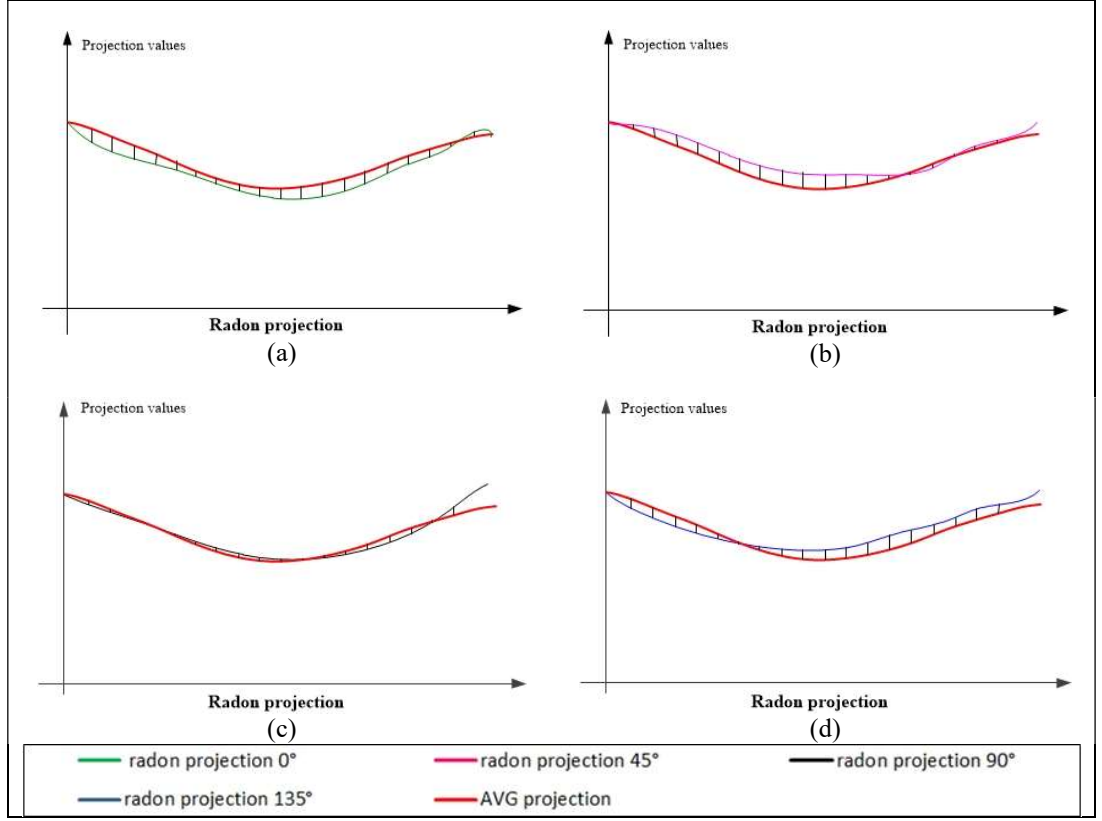


Fig. 12 Radon projections and projection averages for healthy macula with: (a) Angle 0°, (b) Angle 45°, (c) Angle 90°, (d) Angle 135°

Contrarily, the average vector has an important difference with the radon projection, as modeled by the red curvature in Fig. 13. Thus, a full appreciable gap between the profiles of projections and the average projection curvature is provided.

Accordingly, we quantify the distance between the average vector and all radon vectors. Hence, a reduced difference corresponds to a healthy macula where a greater distance is supposed to cause a greater dissimilarity which corresponds to an AMD affected one. Various similarity processing can be used, such as the Mean Square Error (MSE) [37], the M-S similarity[66] and C-LTM[67], which are based on the classical method to calculate the distance vector. In this work, we compute the similarity between the radon projections through the calculation of the MSE between projections, as indicated in Eq. (9). Here, the MSE consists in computing the difference between each radon projection and the average radon space based on the Minkowski distance method [68], as proceeded in [37].

$$MSE = \frac{1}{N \cdot \omega} \sum_{N=1}^N \sum_{\omega=1}^{\omega} (R_{\omega}(N) - \bar{R}(N))^2 \quad (9)$$

where $R_{\omega}(N)$ refers to the (N, ω) component of the radon space, and N and ω are the length of the RT Radon projection and the number of projections respectively.

Thus, for a healthy macula, radon projections have a similar curvature as their average profile, which leads to a lower MSE. In contrast, the drusens involve a differentiated radon projection which leads to a higher MSE. A ω comparison between each RT projection of size n and the mean projection is generated. The, the time complexity of the MSE feature is equal to $O(\omega \times n)$ [37].

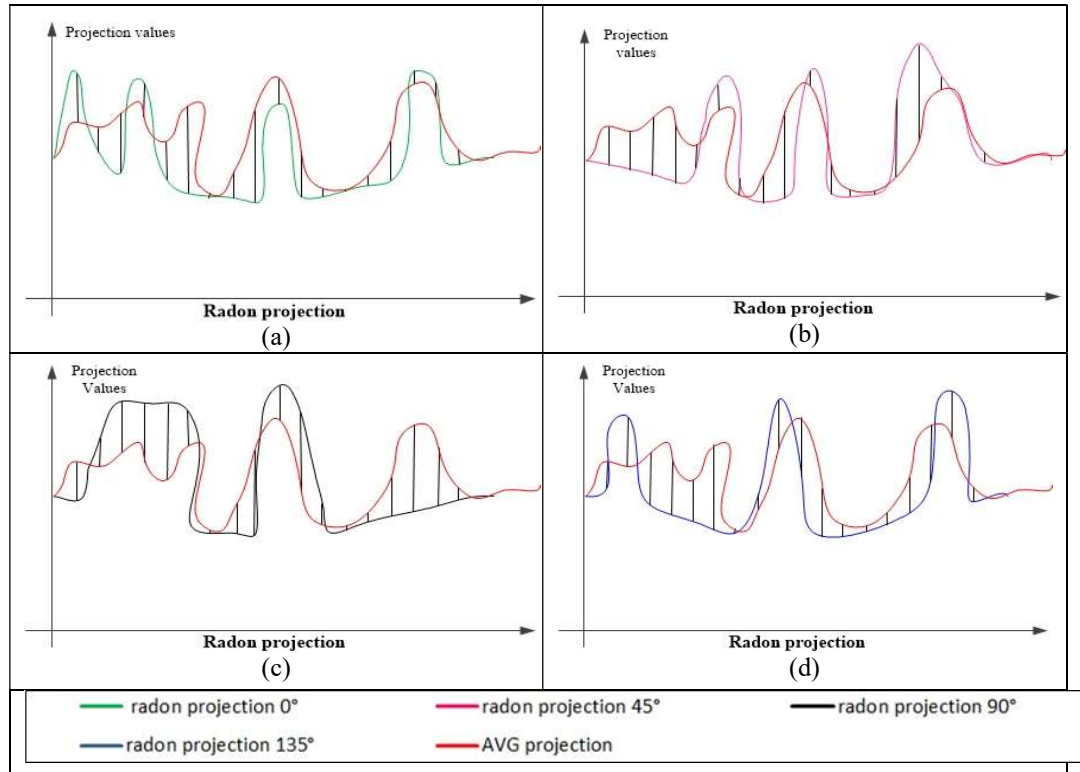


Fig.13 Radon projections and projection averages for AMD affected macula with: (a) Angle 0°, (b) Angle 45°, (c) Angle 90°, (d) Angle 135°

To sum up, different RT projection angles are generated for each sub-image to offer an explicit intensity representation. Then, from the provided radon space, only three adequacy AMD features are identified to reflect all AMD proprieties which are the sample entropy, the dynamic threshold and the MSE. In addition, those features are characterized with lower complexities to achieve a higher computational performance in low execution time. The feature vector will be provided to a classifier to screen the AMD disease, as described in the next sub-section.

3.4 Classification

At this stage, the objective of our method is to combine of the three features of morphological properties to a classifier so as to guarantee an efficient screening in reduced time. To achieve this required classification between healthy and AMD-affected images, several techniques have been used by existing ocular pathology screening methods using different classifiers such as DTs, Naive Bayes, probabilistic neural networks and KNNs[5]. Among those classifiers, the SVM which is a supervised learning machine [69] that demonstrates a higher performance in several ocular pathology classifications, such as the neovascularization detection [70] and the hard exudate detection [71]. The SVM is also reported to be the best performing classifier for AMD screening and AMD severity detection [5, 19, 21]. The work proposed in [72] reported a specificity of 100%, a sensitivity of 99.4% and accuracy of 99.6% using the SVM to classify the testing images. In [19], the authors used an SVM to classify fundus images into healthy/AMD categories and obtained 92.16% accuracy. In [1, 2, 20], it was deduced from the experimentations that the SVM provided better AMD screening performances among different other classifiers. In addition, with respect to the problem of a higher data requirement, the SVM classifier showed a good performance when the training dataset was limited. Moreover, the SVM complexity was between to $C \times d$ and d^2 [73], where C was the number of support vectors which depended on the data set size, and d was the dimensionality of the feature vector,

which was equal to three ones in our case. Hence, a constant time complexity equal to $O(1)$ is required. It is considered as a suitable solution with respect to real-time classification constraints [74]. Consequently, we can infer that the SVM classifier presents an ideal choice for our automated method for AMD screening. Furthermore, the performance of the SVM classifier depends on the kernel type used during the training process. For this purpose, a comparative study is presented in the sub-section 5.2.2 to select an adequate kernel.

In summary, we have proposed in this section a novel method for AMD screening. First of all, we focused on enhancing the contrast in order to properly distinguish between the AMD lesions and the macula background. Then, we have applied the RT at the macula region offering an explicitly intensity representation. Furthermore, we chose the adequacy AMD features for image classification that reflected all AMD properties and we have chosen the SVM in order to ensure the best distinction between healthy and AMD affected images. Table 3 present the complexity of the different step processing and the different features processing used to describe the AMD morphological properties in term of “Irregularity distribution”, “Intensity growth” and “Circular shape distortion”. We focused on carrying out each step processing with lower complexities, which requires a total complexity of $O(\omega \times n^2)$, where $n \times n$ is the input image size and ω is the radon projection number, hence making it adaptable to a mobile implementation.

Table 3 Complexities of AMD Screening steps.

AMD screening steps		Complexity
ROI enhancement		$O(n^2)$
Radon processing		$O(\omega \cdot n^2)$
AMD morphological properties related features	SE	$O(\omega \cdot n^2)$
	Average intensity	$O(\omega \cdot n)$
	MSE	$O(\omega \cdot n)$
SVM Classification		$O(1)$
Total steps of AMD screening method		$O(\omega \cdot n^2)$

4. Smartphone-based AMD screening CAD system

The present work is mainly aimed at deploying a mobile computer-aided system for AMD screening. In this context, the above processing pipeline is running on smartphones as an application.

4.1 Software environment

The entire method is carried out on Android smartphones using the Android Software Development Kit (SDK). The coding for the AMD classification algorithm is performed by combining the Open Computer Vision (OpenCV) library and JAVA programming languages, in order to guarantee computationally efficient execution. OpenCV is an open source computer vision library which can be used with several programming languages such as C, C++ and Python [62]. The OpenCV library contains over than 2,500 optimized image processing functions and is used in a lot of areas as medical imaging, security and multimedia. The OpenCV library also includes a full, general-purpose Machine Learning Library (MLL).

Creating an Android application on the Android platform requires an Android software Native Development Kit (NDK). The NDK is a toolset to work with the Android SDK, which allows compiling the native-code languages such as C and C++ proposed in the OpenCV library. The Android NDK provides the native API compiler system and packages

the native codes into Android Package Kit (APKs) by the integrating Java Native Interface (JNI) with Android SDK. The JNI is used here to enable the JAVA application to embed other language codes, as modeled in Fig. 14.

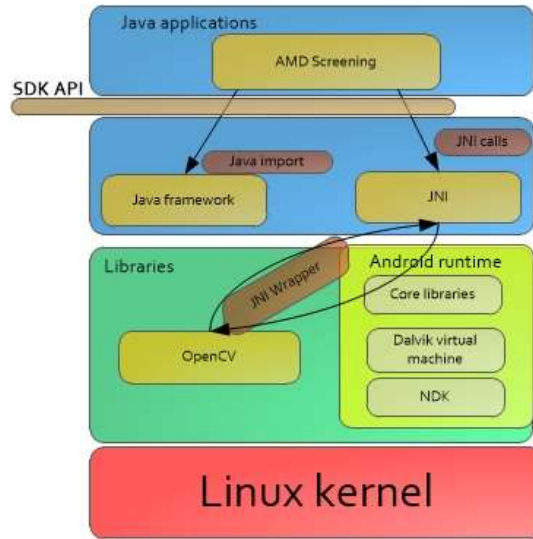


Fig. 14 Android software environment with OpenCV library[75]

4.2 Mobile CAD system for AMD screening

At first, the green channel is extracted and is processed to enhance the contrast using the predefined method in the OpenCV library “*CLAHE.apply()*”, where the image is separated into different regions with a size of 8×8 pixels, which defines using the function “*CLAHE.setTilesGridSize()*”. Thereafter, the RT consists in performing a plane rotation followed by an horizontal and vertical projections [46], where they are applied respectively using predefined functions called “*imrotate()*” and “*core.reduce()*” with parameter “*Core.REDUCE_AVG*”. Then, the three features are implemented using a combination between JAVA trough the Android Studio integrated development environment and native codes defined in OpenCV library. The use of OpenCV enables the use of an SVM classifier on the Android development kit. Accordingly, the SVM classifier is trained with the features extracted from the STARE data base, using predefined function in the Opencv library “*SVM.train()*”. After generating the classification model, it is deployed into mobile CAD system Android smartphones. To do that, the trained model is saved into a check point file. Thereafter, the model is loaded by the mobile CAD system and used for prediction, which allows generation of the classification results. The OpenCV predefined function “*SVM.predict()*” is used to assure AMD screening results.

The graphical user interface illustrated in Fig. 15 allows the selection of the fundus image from the smartphone gallery through the button entitled “Fundus Image Selection”. Afterwards, the second button leads to detect the macula, as indicated by a square added to the fundus images shown in the interfaces of Fig. 15. Next, our proposed method is run through the “AMD Diagnosis” button, where the classification result is provided on the bottom of the graphical interface, as shown in Fig. 15b and Fig. 15c. The application of the entire system is installed on different types of devices where the evaluation time results are described in sub-section 5.4.

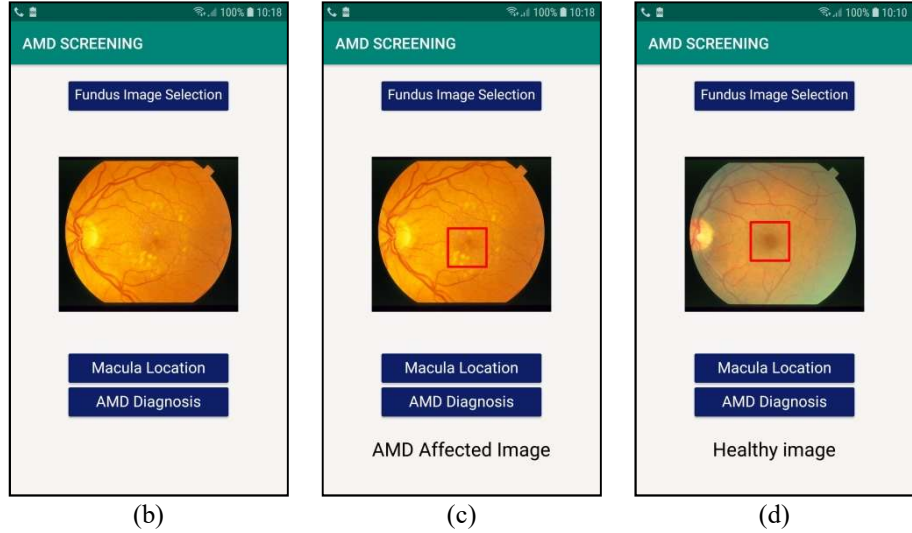


Fig.15 Smartphone graphical interface of AMD classification: (a) Fundus image loading; (b) AMD detection; (c) Healthy image deducing

5. Experiments and results

5.1 Database and evaluation metrics

5.1.1 Databases

To evaluate our proposed method we use the three STARE, REFUGE and RFMiD databases. STARE is a public dataset [74] where images were acquired using a topCon fundus camera at a 35-degree FOV with a size of 700×605 pixels. Each retinal image in STARE dataset was diagnosed as associated to one or more of thirteen different abnormalities. Among several ocular pathologies, the dataset contains fundus affected by AMD which belong to different AMD stages and images corresponding to healthy retinas [19], as indicated in Table 4. A second database "REFUGE dataset" [77], is a public database of 400 fundus images acquired using Zeiss Visucam with a resolution of 1440×1440 pixels. Typical signs of AMD that can be found in AMD images are drusen, exudations, hemorrhages, etc. A third database "RFMiD dataset" [78] contains fundus images taken with three different cameras with a resolution of 2144×1424 , 4288×2848 , 2048×1536 pixels respectively.

We select a fundus image subset from each database containing AMD-affected-fundus images and healthy fundus images, where the labelling was carried out by an expert ophthalmologist. Table 4 shows the number of images in the No AMD and AMD classes and describe the image resolution in each used data set.

Table 4 Image level data base description.

Data bases	Resolution	Number of images per class	
		AMD	No AMD
STARE	700x605	37	27
REFUGE	1440x1440	81	266
RFMiD	2144x1424	169	425
	4288x2848		
	2048x 1536		

5.1.2 Evaluation metrics

The metrics to measure the performance of our method are respectively the True Positive (TP), the True Negative (TN), the False Positive (FP) and the False Negative (FN). The TP

(resp. TN) defines that a macula image is correctly screened as AMD affected (resp. healthy). On the other hand, the FP (resp. FN) consists in classifying a healthy macula (resp. AMD affected macula) as an AMD affected image (resp. healthy image).

Thereafter, we computed the Specificity (Sp) which presents the proportion of correctly-classified healthy macula images among all actual healthy ones, as indicated in Eq.(10). Then, we computed the sensitivity, which indicated the proportion of correctly-classified affected macula images among the actual affected ones, as given in Eq.(11). Likewise, we computed the overall Accuracy (Acc), which presented the proportion of correctly classified macula images among all images (healthy and AMD-affected images), as provided in Eq.(12). The Positive predictive value (PPV), also called precision, denotes the proportion of correctly-classified the AMD affected image among the labeled –affected image and it can be expressed as indicated in Eq. (13). The negative predictive value (NPV) denotes the proportion of correctly-classified healthy subjects among the labeled-healthy ones, as provided in Eq. (14).

$$\text{Specificity} = \text{TN}/((\text{TN}+\text{FP})) \quad (10)$$

$$\text{Sensitivity} = \text{TP}/((\text{TP}+\text{FN})) \quad (11)$$

$$\text{Accuracy} = ((\text{TP}+\text{TN}))/((\text{TP}+\text{TN}+\text{FN}+\text{FP})) \quad (12)$$

$$\text{PPV} = \text{TP}/(\text{TP}+\text{FP}) \quad (13)$$

$$\text{NPV} = \text{TN}/(\text{TN} + \text{FN}) \quad (14)$$

5.2 Feature evaluation

In this section, we evaluate the ability of each feature to distinguish between healthy and AMD-affected images. For this purpose, we study the correlation between the value of each feature and the different classes. Within this objective, we ran our method for the chosen dataset described in the previous sub-section. For each fundus image, we retrieved the three extracted features and the classification result. The SE, dynamic threshold and MSE features are respectively illustrated in Fig 16a, Fig 16b and Fig 16c, where features of a healthy class are represented in a blue color and the features of AMD class are plotted in red.

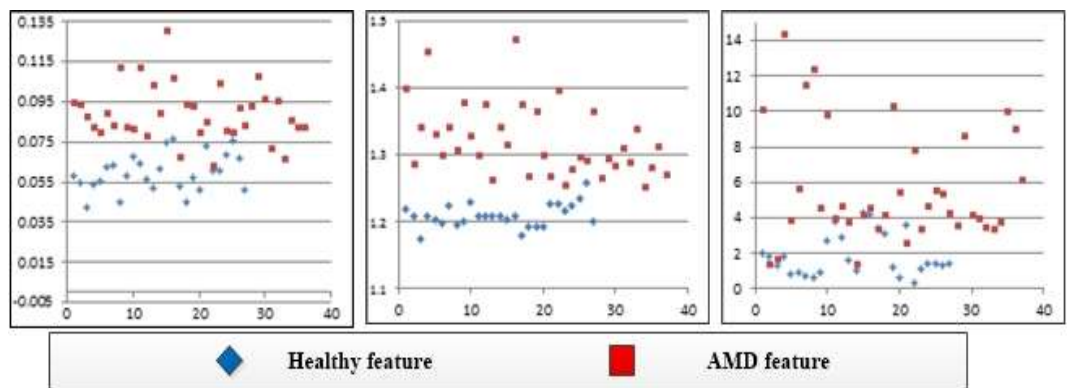


Fig. 16 Feature distribution of healthy and AMD affected maculas: (a) Sample entropy feature, (b) Dynamic threshold based intensity rate feature, (c) MSE feature

It is easy to deduce that the features are effective for reflecting the AMD disease in the fundus images. The three features raise values in most of AMD affected images related respectively to the high variation in the radon projection, the presence of the high peaks and the dissimilarity between the radon projections caused by the presence of drusens.

The overlapped values of features between a healthy and an affected macula are reported, like the exceptional cases mentioned in the sub-section 3.3. However, the features seem complementary in order to provide a performing AMD classification. For example, the drusens of the late AMD stage, represented by images 17 and 22, are expanded to gather and appear as a large one in a circular form. Consequently, low SE and MSE values are reported. In this case, the dynamic threshold based intensity rate proposes a complementary feature, where the coalesced of multi-drusens provides high intensity values, hence producing a good classification performance.

5.3 Evaluation of AMD screening method on unbalanced datasets

In this section, we choose the SVM kernel that allows achieving a higher detection performance. In order to efficiently evaluate our proposed method, we put forward a 4-fold cross validation approach, which consists in partitioning the retinal images of each dataset into four subsets in order to perform four experiments for each dataset. For each experiment, three subsets are conducted for the training process and one subset for testing. We extract the features of all fundus image datasets, to be used for training and test processes. Then, we experimentally test the classifier with three different kernels that are respectively the linear, the RBF and the polynomial, where the achieved accuracy using STARE data set, REFUGE data set and RFMD data set. Table 5 lists the average results of the SVM classifier measures for 4-fold cross validation.

We note that classifier parameters offering the better performance are chosen through the SVM auto-train algorithm [79], which is widely used and considered by the most accurate optimization technique.

Table 5 SVM classifier measure for 4-fold cross validation for imbalanced STARE, REFUGE and RFMiD datasets using various SVM kernels.

Data bases	Classifiers	Metrics				
		Accuracy	Specificity	Sensitivity	PPV	NPV
STARE	SVM with RBF kernel	100%	100%	100%	100%	100%
	SVM with linear kernel	96.2%	90.9%	100%	93.75%	93.75%
	SVM with polynomial kernel	100%	100%	100%	100%	100%
REFUGE	SVM with RBF kernel	85.7%	89,36%	66,66%	54,54%	93,33%
	SVM with linear kernel	84.3%	86,20%	75,0%	52,94%	94,33%
	SVM with polynomial kernel	84.3%	85.71%	80%	47%	96,22%
RFMiD	SVM with RBF kernel	85.7%	83.16%	100%	51.42	100
	SVM with linear kernel	84.9%	82.35%	100%	48.57%	100
	SVM with polynomial kernel	85.7%	83.83%	95%	54.28%	98.80

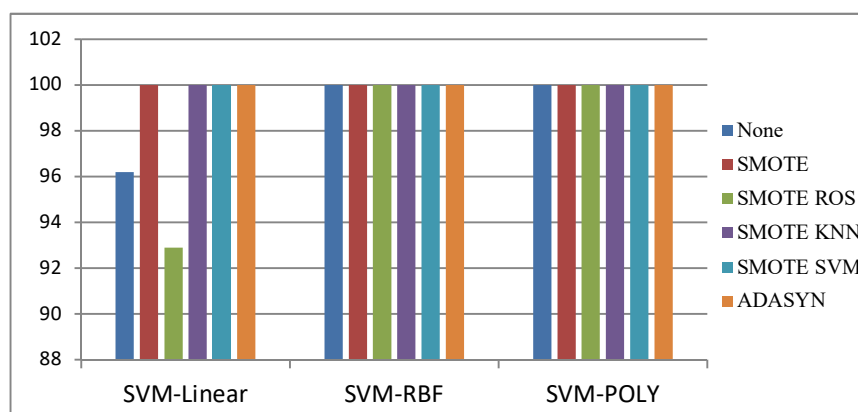
We can see that the accuracy values provided by the validation of STARE database are very close in the different kernel, as highlighted by the average performance values in table 5. It is deduced that the RBF kernel allow achieving the highest performance rate in average fold cross of REFUGE and RFMiD datasets, which will be chosen for our method. However, large gap are deduced between classification performances of the REFUGE and RFMiD databases, which are unbalanced, with minority classes having fewer fundus images. Several studies have affirmed that unbalanced dataset affects the classification and decreases the accuracy rate [21, 80].

5.4 Oversampling techniques for unbalanced dataset issue

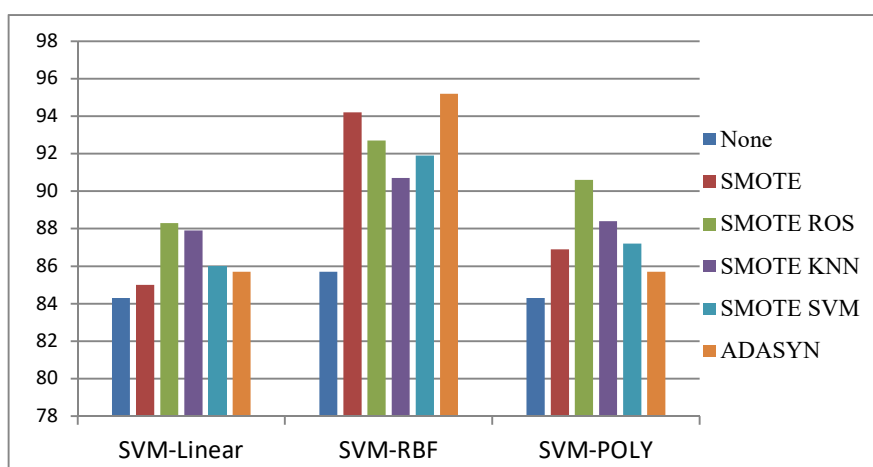
To address unbalanced dataset problem, an oversampling preprocessing technique should be applied to unbalanced datasets before the classification process. Several resampling techniques have been proposed in the literature to overcome this problem before the classification process [21, 80–85]. Those oversampling techniques differ, according to their principle of dealing with class imbalance or adding new synthetic minority instances. To this end, we proceed to evaluate different techniques. Then, the Friedman signed rank test is applied, in order to select the best performing oversampling technique.

5.4.1 Evaluation of AMD screening method with oversampling technique

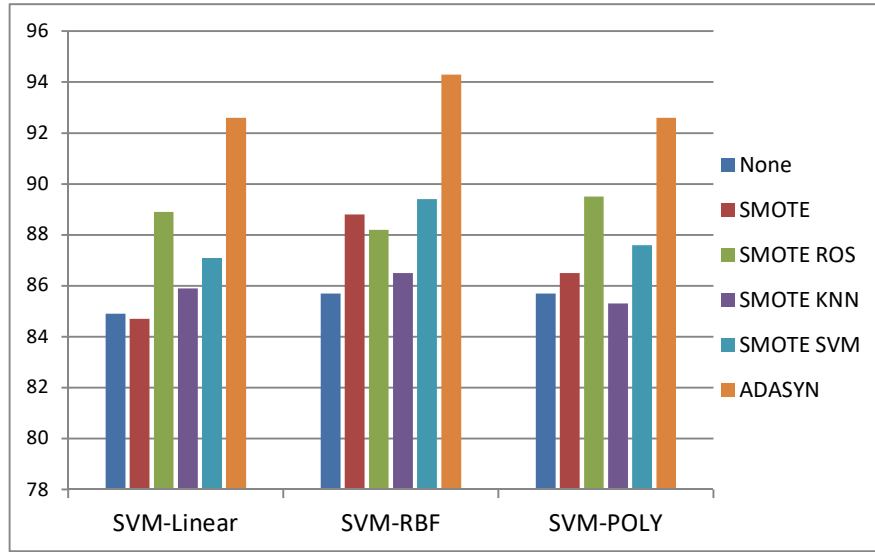
This experimentation was applied on each dataset, where the different techniques used were compared. In order to avoid overfitting, 20% of the generated data is used as test set. Figure 17 summarizes the performance accuracy on the three datasets without any resampling and by applying the five previous oversampling techniques, where NONE denotes the experimental results without oversampling. In all the tests, the datasets have been balanced, decreasing the final imbalance until the same number of samples for both classes is obtained. In order to demonstrate the efficiency of the proposed method, the classification performances of SVM classifier kernels are compared. The training of the classifiers is performed by using the obtained resampled dataset generated by the different oversampling techniques.



(a)



(b)



(c)

Fig. 17: The performance measurements using various SVM classifier kernels on (a) STARE dataset without any resampling and by applying oversampling techniques (b) REFUGE dataset without any resampling and by applying oversampling techniques, and (c) RfMiD dataset without any resampling and by applying oversampling techniques.

This result shows that by balancing the number of samples in the different classes, the classification error is minimized, thus allowing us to increase the classification performance. From Figure 17, we can see that the majority oversampling algorithms enhance accuracy. Knowing that oversampling techniques provide different results, the Friedman signed rank test [86] was applied based on the accuracy performance as presented in Table 6.

Table 6 : Results of Friedman’s rank test between the different oversampling techniques.

Techniques	SVM-Linear	SVM-RBF	SVM-Poly
None	4.3333	4.3333	4
SMOTE	4	2	3
SMOTE ROS	2	2.6666	1.3333
SMOTE KNN	2.3333	3.6666	3
SMOTE SVM	2.3333	2.3333	2.3333
ADASYN	2	1	2.3333

We can observe that the average ranks of the majority oversampling algorithms are obviously lower than NONE. In addition, we note that there are significant differences among oversampling technique, which prove that the influence of resampling depends strongly on the resampling technique. We deduce that "ADASYN" technique always has the best average rankings using the linear and RBF SVM classifiers. Further, the training of the SVM-RBF classifiers with the obtained from "ADASYN" technique, leads to achieve the highest performances using the different data sets. Accordingly, the "ADASYN" over sampling technique coupled with SVM-RBF classifier are the adequate ones to solve the nonlinear boundary classification problems of our extracted features.

5.5 Performance evaluation of AMD screening method with respect to the state-of-the-art methods

In this step, we aim to compare the performance of our method to the existing ones. In this comparison, the STARE, REFUGE and RfMid databases were balanced with "ADASYN"

technique and were classified by SVM-RBF. This comparison is ensured based on the sensitivity, specificity and accuracy metrics. Table 7 highlights the performance validation of our proposed method to state-of-art approaches using same dataset, where the best results are shown in bold.

First, recent works, whose evaluation has been based on the STARE database, are selected. Despite having used the same dataset, we obtained the highest classification accuracy of 100, sensitivity of 100 and specificity of 100, among some previous work [2, 19, 20] that reported accuracy of 93.60, 92.15 and 82.92 respectively. It is important to highlight that our method uses 3 significant features to obtain an average accuracy of 100, whereas the literature [1] and [17] used 1262 and 30 features respectively and used the ranking test and feature selection algorithm to obtain the same accuracy. We use the box plots to present the performance of these experiments, as shown in Figure 18A. These box plots demonstrate high performances in terms of accuracy, sensitivity and specificity.

Table 7 Performance detection of AMD screening in terms of existing methods

Data base	Works	Metrics				
		Accuracy	Sensitivity	Specificity	NPV	PPV
STARE	Mookiah et al., 2014a[20]	82.92	88	71.67	NA	86.10
	Mookiah et al., 2015b[2]	93.6	98.00	97.50	NA	97.87
	Mookiah et al., 2015a[1]	100	100	100	NA	97.8
	Acharya et al., 2016[17]	100	100	100	NA	100
	García-Florianio et al., 2019[19]	92.15	88.2	NA	NA	93.2
	Samina Khalid et al 2021[87]	95.45	97.5	95	98	91
	Our proposed work	100	100	100	100	100
REFUGE	V. Rajinikanth et al 2021 [88]	93.67	93.33	94.00	93.38	93.96
	Our proposed work	95.2	100	88.23	100	92.59
RFMiD	Wang Heyang [89]	72.55	--	--	--	--
	Our proposed work	94.3	95,18	93,47	95,55	92,94

Subsequently, our method is evaluated using the REFUGE dataset, and achieves a classification accuracy of 95.2%, a sensitivity of 93.33% and a specificity of 100%. As indicated in table 7, the performance measures are not high as compared to Stare dataset. The reason of the variations in accuracy may be due to the presence of different abnormal lesions. As described in section 5.1.1, lesions in the REFUGE data set are large as compared to STARE dataset. In addition, the non-AMD images in the REFUGE dataset contained healthy images and images with different anomalies. Even through this challenged data base, the success rates of our method are compared with those of other methods [88] which used the same data set and clearly indicate the high performance of the proposed method. The different performances are modeled through the box plots illustrated in Fig. 18B. The sensitivity of 100% presented in the fourth column of table 7 indicates a successful discriminating power while separating AMD affected image from the normal images.

Finally, our method is evaluated using the RFMiD database. To our knowledge, we are the first paper to have evaluated the proposed method with this challenged database for AMD prediction, and achieve a classification accuracy of 94.3%, a sensitivity of 95.18% and a

specificity of 93.47%, as presented in the last line of table 7. The different performances are modeled through the box plots illustrated in Figure 18.C. The performance measures are not high as compared to STARE dataset. The reason of the variations in accuracy may be due to the presence of different abnormal lesions in the AMD fundus image, as described in section 5.1.1. A success rates of our method are compared with other method [89], based on deep Learning for different pathologies recognition, which used the same dataset. The proposed method clearly shows the high performance. The results also show that the proposed method has significant features that well describe the properties of drusen compared to other retinal regions.

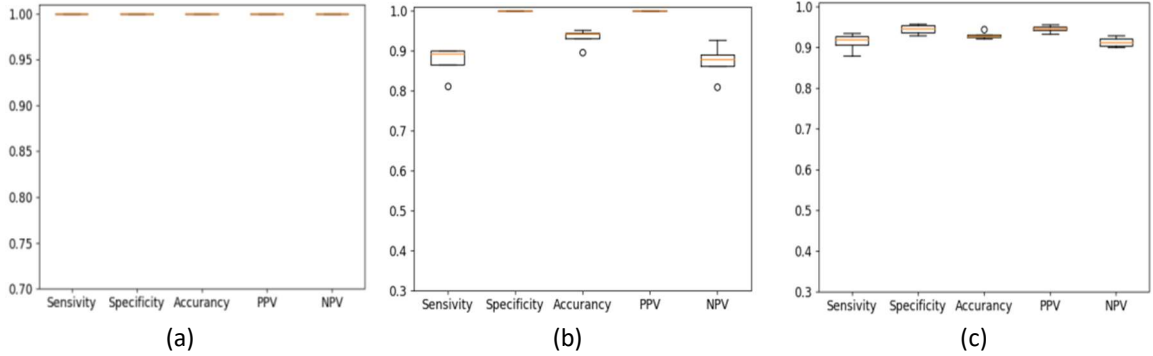


Fig. 18 Performance visualization using box plots: (a), Stare fundus images dataset; (b), REFUGE fundus image dataset, (C), RFMID fundus image dataset

5.6 Robustness evaluation of AMD screening method

At this stage, we aim to prove the robustness of our method, even the moderate quality of SCFIs. In fact, the capture of fundus images using smartphones leads to a light leakage, which produces noises in fundus images. Moreover, the handled aspect of smartphones decreases the image quality and produces a blur in fundus images. Thus, the main idea is to apply a processing to the classical fundus image in order to reproduce degraded fundus images similar to the ones captured with smartphones. Within this framework, we generate a new dataset through applying data augmentation to the dataset described in the sub-section 5.1. For each fundus image, blurring and noising using respectively a Gaussian blur and a Gaussian noise were applied. Accordingly, a second dataset was provided which was composed of 35 blurred and 35 noised AMD affected images, and 27 blurred and 27 noised healthy images.

In figure Fig.19, we investigated the correlation between quality degradation and the ability of the radon space to reflect the macula image. The experimentation consists of generating the radon space using the 180 radon projection, to healthy and AMD-affected macula image. The macula depicted in Fig19 (b) and Fig19 (c) are provided after applying the motion blur filter and Gaussian noise filter respectively, in the macula showed in Fig19 (A). We can highlight that despite the loss of information caused by the blurred filter, the meaningful preprocessing that we put forward succeeded in avoiding the unbalanced contrast problem of the macula image. Added to that, the RT robustness to noise enables us to overcome the problem of a degraded quality of fundus images. We can see that the Radon Projection leads to reflect explicitly the macula texture with a higher precision. The radon spaces maintain reflecting the drusens properties through the valleys inside the radon space and the higher irregular distribution of intensity. In the case of healthy macula, we can see that the semi-cylindrical shape all radon spaces are conserved, as well as the regular variation of contrast.

(a)	(b)	(c)
-----	-----	-----

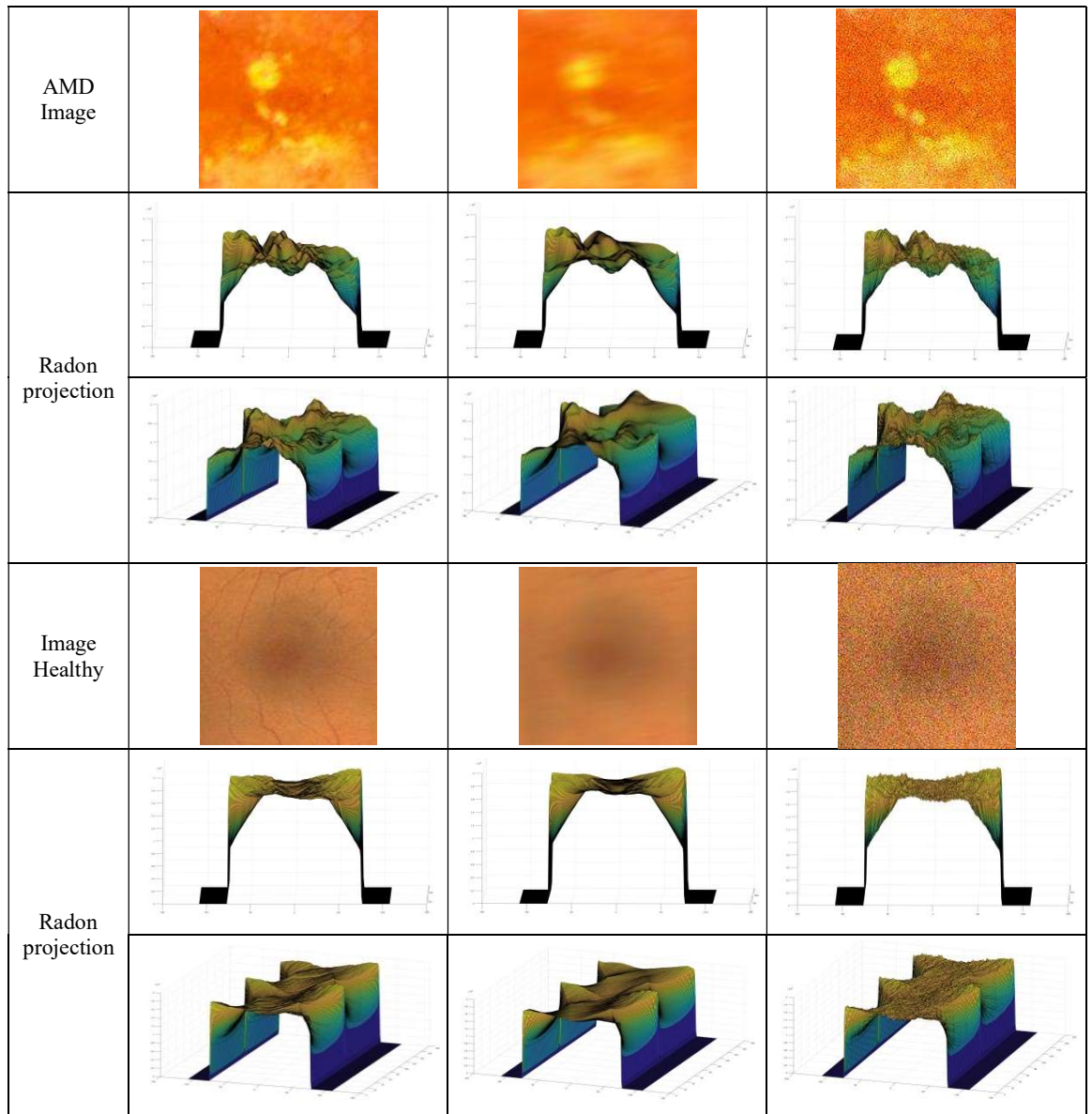


Fig .19 Radon space with different view of healthy and AMD affected macula; (a) original image, (b) Blurred image, (c) Noised image.

Following this, the proposed method was evaluated using the second dataset which included original, noisy and blurred images, the performance of which is shown in Table 8. In this experimentation, we put forward a 5-fold cross validation approach, which consists in partitioning the retinal images of original and degraded Stare database into five subsets in order to perform five experiments. The goal of these experiments is to efficiently evaluate the robustness of the suggested method. In each experiment, three subsets, subsets that are indicated in green in Fig 20, are conducted for the training process and two subsets for testing. Fig. 20 shows the dispatching of subsets between training and testing of each experiment.

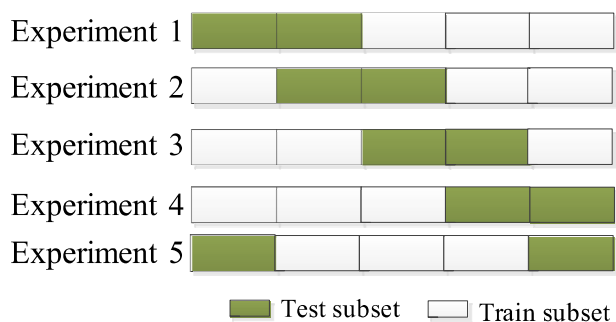


Fig . 20 Dispatching of subsets for 5-fold cross validation.

As a result, our methods maintained the same accurate accuracy of 100% for the original STARE data base for 5-fold cross validation, even with the reduced number of images used for the training process, as illustrated in Fig 21. Consequently, the proposed method confirms a higher performance whatever the number of image used for the training or testing procedure.

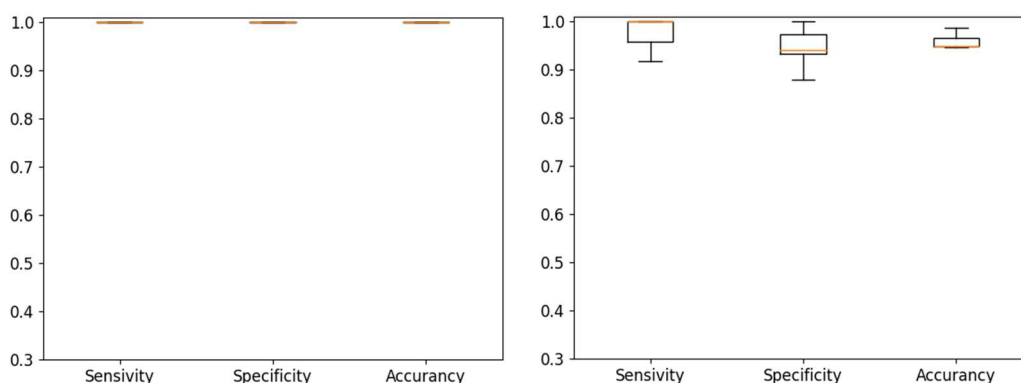


Fig. 21 Performance visualization for 5-fold cross validation using box plots: (a), Stare fundus images dataset; (b), Stare dataset with degraded quality fundus image

Table 8 carried out the mean of the evaluation measures obtained on five different test subsets. A productive performance are achieved, where the average accuracy, sensitivity, specificity are respectively in the order of 95.2%, 97.9% and 93.8%, for the degraded quality of fundus images. These results prove the robustness of our method and confirm its ability to predict the AMD affected image even with an original or degraded image. Furthermore, this aspect proves the performance of our method, which is suitable for clinical use, and confirms its ability to be used on a mobile CAD system.

Table 8 Average performance measures for 5-fold cross validation of suggested method in terms of original and degraded quality of fundus images.

Databases	Metrics		
	Accuracy	Sensitivity	Specificity
Original STARE dataset	100%	100%	100%
Degraded quality fundus image dataset	95.2%	97.9%	93.8%

5.7 Real time implementation of AMD detection on mobile devices

The CAD system is designed to run on different types of devices, in order to prove the standalone capability in different computing power and memory resources. For that, we implemented our method on two different smartphone devices, where their hardware features are listed in Table 9.

Table 9 Hardware features of implementation platforms.

Model	Samsung Galaxy S7-edge	Samsung Galaxy S9
CPU architecture	Samsung Exynos 8890	Samsung Exynos 9810
CPU number	8 core	8 core
CPU frequency	2.3GHz	2.7 GHz
RAM	4Go	4Go
OS	Android v6.0 (Marshmallow)	Android v8.0 (Oreo)

5.7.1 Execution time evaluation

In this section, we investigate the execution time of each processing step of the proposed method. Table 10 figured out separately the execution time of all method steps with RT projection with step values equal to 1° on the S7-edge and S9 smartphone. We deduce that the whole method implementation is run on 68 ms and 100 ms respectively in "Samsung S9" and "Samsung S7-edge".

As highlighted in Table 3, the processing of "ROI enhancement", "average intensity", "MSE" and "SVM-RBF prediction" have a complexity of $O(\omega.n)$. Similarly, their low processing workload leads to low execution times not exceeding 2 ms for each of them for both Smartphone S7-Edge and S9. However, it can be noted that the two processes "Radon projection" and "SE" represent a large complexity of $O(\omega.n^2)$. Furthermore, they achieve higher execution time equal to 41ms and 54 ms (resp. 35 and 29) for S7-Edge (resp. S9).

Table 10 AMD screening execution time with RT projection with step values equal to 1° : (a) on S7-edge ; (b) on S9

Method of AMD screening steps		Execution Time (ms)	
		Samsung Galaxy S7-edge	Samsung Galaxy S9
ROI enhancement		2	1
Radon processing		41	35
AMD morphological property related features	SE	54	29
	Average intensity	1	1
	MSE	1	1
Classification	SVM-RBF	1	1
Whole method of AMD screening		100	68

Indeed, both "radon projection" and "SE" require an iterative processing in terms of projection number w , which explains their higher execution time. Elsewhere, the size growth of input images leads to a similar growth on computational time. This rise cannot be resolved through the evolution of smartphones in terms of processing power and memory capacities. Hence, those processings are impeding the use of AMD screening methods in a clinical context.

5.7.2 Optimization of AMD screening Algorithm

The objective of the optimization approach is to reduce the execution time of the proposed method in order to achieve a real-time implementation. To consider the distribution of drusens in all directions, the radon spaces of healthy and AMD-affected images are generated using a maximal number of radon projections, performed from 0° to 179° with step values equal to 1° . However, with respect to the time complexities illustrated in Table 3, the complexity of both "Radon projection" and "SE" processes depends on the radon projection number. As a consequence, a higher projection number, $\omega=180$, involves a similar rise in the execution time.

As deduced in the sub-section 3.2, generating a radon space where projection angles are too close produces a similar projection. This aspect is confirmed when observing Fig. 22a and Fig. 22b which contains projections of an AMD-affected image where the radon

vectors have the same shape. Hence, higher excessive redundancy features are extracted based on the generation of the radon space with an angle step equal to 1° .

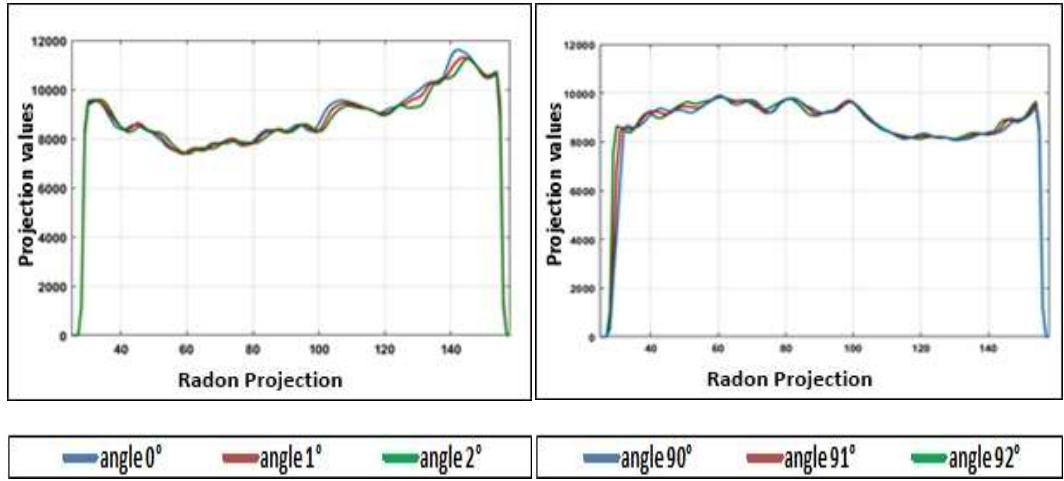


Fig. 22 Radon projections of AMD affected macula: (a) at angles $0^\circ, 1^\circ$ and 2° ; (b) at angles $90^\circ, 91^\circ$ and 92°

Thus, we aim to reduce the number of radon projections w and evaluate the correlation between the number of radon projections and the ability to detect AMD. Within this scope, we propose an optimization approach where the number of radon projections w of both "Radon projection" and "SE" processes is reduced iteratively, while maintaining an optimal performance of 100%, as depicted in Fig. 23.

In the first part modeled by a red square in Fig. 23, the approach consists in reducing the radon projection number ω required in the whole method. Thereby, the optimal radon space was generated using a maximal number of radon projections equal to 180. Then, the method implementation was performed and evaluated using the STARE fundus image set. Thereafter, we reduced the number of projections, ω iteratively and investigated the performance of the AMD detection in each one. The provided ω is the last one maintaining the higher 100% accuracy.

The second part, illustrated in a blue square in Fig. 23, aims to reduce the radon projection number taking into account to compute the SE computation, called ω_{SE} . Within this objective, we iteratively varied ω_{SE} in terms of selected number of radon projections ω . In each variation, we adopted new SE measures and evaluated the accuracy of the AMD screening method. Similarly, the provided ω_{SE} is the last one maintaining the higher 100% accuracy.

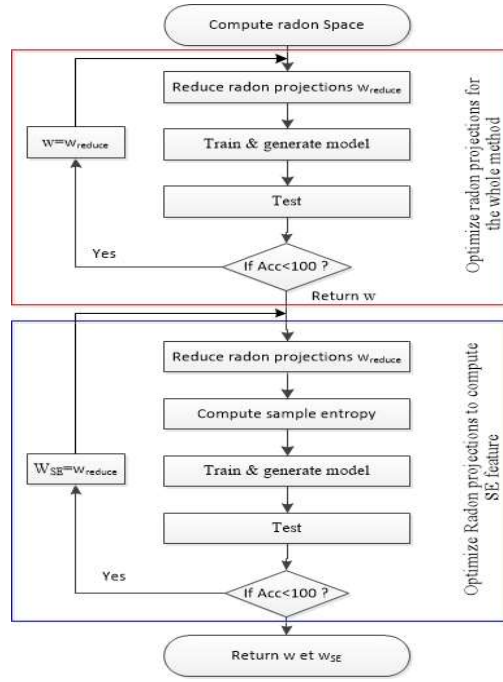


Fig. 23 Optimization approach for identifying optimal number of radon projection

5.7.3 Optimization of number of radon projection for whole method

It can be deduced that even with a reduced radon projection number the radon spaces maintain the reflecting properties of drusens. Table 11 (resp Table 12) present some accuracy and execution time of processing steps “Radon processing” and “Sample entropy” in terms of Radon projection number ω on the S7-edge (resp S9) smartphone. It was observed that 100% accuracy was maintained while reducing the radon projection number until achieving $\omega = 45$. However, we noted that the AMD screening accuracy decreased continuously to achieve 98.8% when $\omega = 36$.

Table 11 Impact of reducing RP number of radon projection processing execution time on Smartphone S7-edge

Method of AMD screening steps		S7-edge					
Radon projection number		$\omega = 180$	$\omega = 120$	$\omega = 90$	$\omega = 60$	$\omega = 45$	$\omega = 36$
Execution time (millisecond)	Radon processing	41	28	21	14	11	7
	Sample entropy	54	38	26	18	14	11
	Whole method	100	71	50	35	30	23
Accuracy (%)		100	100	100	100	100	98.8

A decreasing projection number ω leads to a linear fall in the execution time for the whole method. In fact, the ROI enhancement, the “average intensity”, the “MSE” and the “SVM-RBF prediction” processing are characterized by a low processing workload that results in an insignificant modification on their execution time. Nevertheless, the execution time of the radon and SE processing were reduced from 41 and 54 (resp. 35 and 29) to 11 and 14 (resp. 9 and 8) for the S7-Edge (resp. S9), as presented in Table 11 (resp Table12). Consequently, real time AMD screening was achieved where the execution time of 30 and 21 milliseconds is registered in S7-Edge and S9, which was optimized as described in the following sub-section.

Table 122 Impact of reducing RP number of radon projection processing execution time on Smartphone S9

Method of AMD screening steps		S9					
Radon projection number		$\omega = 180$	$\omega = 120$	$\omega = 90$	$\omega = 60$	$\omega = 45$	$\omega = 36$
Execution time (millisecond)	Radon processing	35	21	17	12	9	6
	Sample entropy	29	20	11	10	8	6
	Whole method	68	49	32	26	21	16
Accuracy (%)		100	100	100	100	100	98.8

5.7.4 Optimization of selected radon projection for sample entropy extraction

In the second experiment, we iteratively varied ω_{SE} in terms of selected number of radon projection $\omega = 45$. This variation was performed within the division of the radon projection iteratively. The AMD detection accuracy and the execution time of the SE processing and the whole method are illustrated in Fig. 24.

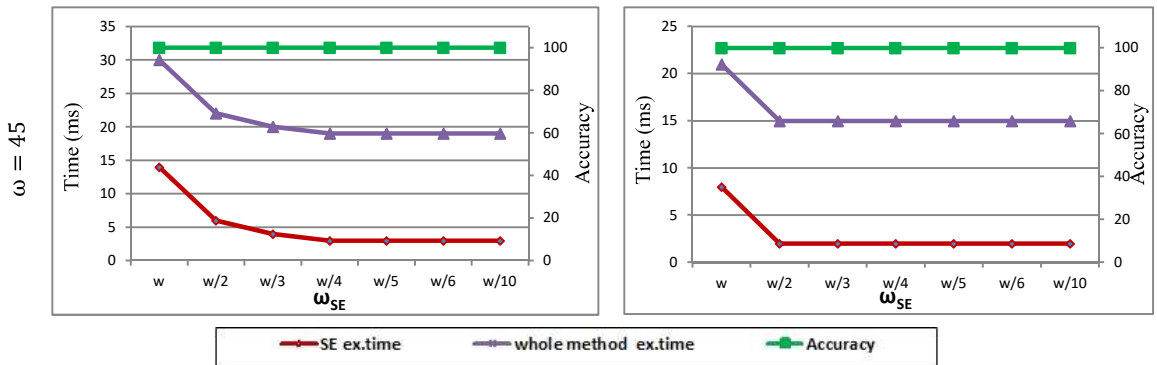


Fig. 24 Execution time of the SE processing and the AMD screening method in terms of radon projection number and mobile devices

We deduce that reducing ω_{SE} when computing the SE feature ensures adequately reflecting the irregularity of the radon space. Moreover, it leads to a significant decrease in the execution time, achieving 2 and 3 milliseconds respectively in S7-Edge and S9, where it is more stable for $\omega_{SE} = w/10$. Knowing that the SE processing has a complexity of $O(\omega.n^2)$, similar to the whole method complexity, the execution time decrease in the SE processing implies a similar fall in the whole execution time, confirmed through the curve slopes. Similarly, a slight reduction in ω_{SE} relies on the decreased execution time. Table 13 shows the provided execution time, speed up and Fps of the selecting number of radon projections ω and ω_{SE} on the S7-edge and S9 smartphone. We can observed that the execution time of AMD screening achieved 19 and 15 milliseconds in S7-Edge and S9, which corresponds to speedups of 5.26 and 4.53. Hence, AMD screening can be performed through 52 Fps and 66 Fps, respectively, which allows a higher quality of real time detection through a video stream.

Table 13 Computational performance of proposed method with optimal radon projection number.

	S7-edge		S9	
	$(\omega = 45)$ $(\omega_{SE} = \omega)$	$(\omega = 45)$ $(\omega_{SE} = \omega/10)$	$(\omega = 45)$ $(\omega_{SE} = \omega)$	$(\omega = 45)$ $(\omega_{SE} = \omega/10)$
Execution time (ms)	30	19	21	15
Speedup	3.33	5.26	3.24	4.5
Frame per second (Fps)	33	52	47	66

6 Conclusion

Regular eye screening helps diagnose AMD and may prevent vision loss in the elderly. As part of this work, a method for the detection of drusen using fundus images is suggested to assist ophthalmologists in the prevention of AMD. This method consists in enclosing the macula in a ROI. Then, the intensity of the macula is modeled using RT. Three features are then extracted from the radon representation based on the properties of AMD. The reduced number of features allows this algorithm to run efficiently on Android smartphones. In order to achieve the higher performance of the classification, a synthetic oversampling technique is used to balance the number of features between classes, where it is selected based on non-parametric statistically test named Friedman's. The proposed method was implemented on android smartphone and achieved an average accuracy of 100%, 95.2% and 94.3% respectively for STARE, REFUGE and RFMiID databases using an SVM-RBF classifier coupled with the ADASYN oversampling technique. Thus, the implementation proved its robustness using a degraded image quality. Moreover, the method was implemented in S7-edge and S9 smartphone devices where the execution time of 19 and 15 milliseconds were achieved.

This work can be provided as a CAD system for ophthalmology to take advantage of its mobility, cost-effective, detection performance and reduced execution time. It can be used worldwide to decrease the overload of ophthalmologists. It can also be used in rural areas where ophthalmology care is limited. Although the suggested method proves its robustness for degraded image quality, it is necessary to enrich the learning of SVM classifiers with smartphone captured images. For that, future work will focus on exploring the detection of AMD on other databases which contain smartphone captured images.

7 Acknowledgements

Funding for this study came from Campus-France through the PHC-UTIQUE Research program (grant number: 19G1408). The authors acknowledge the help of Dr. Nesrine Abroug, ophthalmologist in the hospital Fattouma Bourguiba (Tunisie), to provide the ground truth of smartphone-captured fundus images.

Reference

1. Mookiah, M. R. K., Acharya, U. R., Fujita, H., Koh, J. E. W., Tan, J. H., Chua, C. K., ... Tong, L. (2015). Automated detection of age-related macular degeneration using empirical mode decomposition. *Knowledge-Based Systems*, 89, 654–668. <https://doi.org/10.1016/j.knsys.2015.09.012>
2. Mookiah, M. R. K., Acharya, U. R., Fujita, H., Koh, J. E. W., Tan, J. H., Noronha, K., ... Tong, L. (2015). Local configuration pattern features for age-related macular degeneration characterization and classification. *Computers in Biology and Medicine*, 63, 208–218. <https://doi.org/10.1016/j.compbiomed.2015.05.019>
3. Wong, W. L., Su, X., Li, X., Cheung, C. M. G., Klein, R., Cheng, C.-Y., & Wong, T. Y. (2014). Global prevalence of age-related macular degeneration and disease burden projection for 2020 and 2040: a systematic review and meta-analysis. *The Lancet Global Health*, 2(2), e106–e116. [https://doi.org/10.1016/S2214-109X\(13\)70145-1](https://doi.org/10.1016/S2214-109X(13)70145-1)
4. Köse, C., Şevik, U., Gençlioğlu, O., İkibaş, C., & Kayıkçıoğlu, T. (2010). A Statistical Segmentation Method for Measuring Age-Related Macular Degeneration in Retinal Fundus Images. *Journal of Medical Systems*, 34(1), 1–13. <https://doi.org/10.1007/s10916-008-9210-4>
5. Pead, E., Megaw, R., Cameron, J., Fleming, A., Dhillon, B., Trucco, E., & MacGillivray, T. (2019). Automated detection of age-related macular degeneration in color fundus photography: a systematic review. *Survey of Ophthalmology*, 64(4), 498–511. <https://doi.org/10.1016/j.survophthal.2019.02.003>
6. Köse, C., Şevik, U., & Gençlioğlu, O. (2008). Automatic segmentation of age-related macular degeneration in retinal fundus images. *Computers in Biology and Medicine*, 38(5), 611–619. <https://doi.org/10.1016/j.compbiomed.2008.02.008>
7. Remeseiro, B., Barreira, N., Calvo, D., Ortega, M., & Penedo, M. G. (2009). Automatic Drusen Detection from Digital Retinal Images: AMD Prevention. In R. Moreno-Díaz, F. Pichler, & A. Quesada-Arencibia (Eds.), *Computer Aided Systems Theory - EUROCAST 2009* (pp. 187–194). Berlin, Heidelberg: Springer. https://doi.org/10.1007/978-3-642-04772-5_25

8. Almahdi, E. M., Zaidan, A. A., Zaidan, B. B., Alsalem, M. A., Albahri, O. S., & Albahri, A. S. (2019). Mobile-Based Patient Monitoring Systems: A Prioritisation Framework Using Multi-Criteria Decision-Making Techniques. *Journal of Medical Systems*, 43(7), 219. <https://doi.org/10.1007/s10916-019-1339-9>
9. Thabtah, F., Mampusti, E., Peebles, D., Herradura, R., & varghese, jithin. (2019). A Mobile-Based Screening System for Data Analyses of Early Dementia Traits Detection. *Journal of Medical Systems*, 44(1), 24. <https://doi.org/10.1007/s10916-019-1469-0>
10. Teo, J. (2020). Early Detection of Silent Hypoxia in Covid-19 Pneumonia Using Smartphone Pulse Oximetry. *Journal of Medical Systems*, 44(8), 134. <https://doi.org/10.1007/s10916-020-01587-6>
11. Naik, B. N., Gupta, R., Singh, A., Soni, S. L., & Puri, G. D. (2020). Real-Time Smart Patient Monitoring and Assessment Amid COVID-19 Pandemic – an Alternative Approach to Remote Monitoring. *Journal of Medical Systems*, 44(7), 131. <https://doi.org/10.1007/s10916-020-01599-2>
12. Akil, M., & Elloumi, Y. (2019). Detection of retinal abnormalities using smartphone-captured fundus images: a survey. In *Real-Time Image Processing and Deep Learning 2019* (Vol. 10996, p. 109960K). Presented at the Real-Time Image Processing and Deep Learning 2019, International Society for Optics and Photonics. <https://doi.org/10.1117/12.2519094>
13. Mohammadpour, M., Heidari, Z., Mirghorbani, M., & Hashemi, H. (20171207). Smartphones, teleophthalmology, and VISION 2020. *International Journal of Ophthalmology*, 10(12), 1909–1918. <https://doi.org/10.18240/ijo.2017.12.19>
14. Jin, K., Lu, H., Su, Z., Cheng, C., Ye, J., & Qian, D. (2017). Telemedicine screening of retinal diseases with a handheld portable non-mydratric fundus camera. *BMC Ophthalmology*, 17(1), 89. <https://doi.org/10.1186/s12886-017-0484-5>
15. Volk Optical. (n.d.). Volk Optical. Retrieved August 21, 2020, from <https://www.volk.com/>
16. Majumder, S., Elloumi, Y., Akil, M., Kachouri, R., & Kehtarnavaz, N. (2020). A deep learning-based smartphone app for real-time detection of five stages of diabetic retinopathy. In *Real-Time Image Processing and Deep Learning 2020* (Vol. 11401, p. 1140106). Presented at the Real-Time Image Processing and Deep Learning 2020, International Society for Optics and Photonics. <https://doi.org/10.1117/12.2557554>
17. Acharya, U. R., Mookiah, M. R. K., Koh, J. E. W., Tan, J. H., Noronha, K., Bhandary, S. V., ... Laude, A. (2016). Novel risk index for the identification of age-related macular degeneration using radon transform and DWT features. *Computers in Biology and Medicine*, 73, 131–140. <https://doi.org/10.1016/j.combiomed.2016.04.009>
18. Rapantzikos, K., Zervakis, M., & Balas, K. (2003). Detection and segmentation of drusen deposits on human retina: Potential in the diagnosis of age-related macular degeneration. *Medical Image Analysis*, 7(1), 95–108. [https://doi.org/10.1016/S1361-8415\(02\)00093-2](https://doi.org/10.1016/S1361-8415(02)00093-2)
19. García-Floriano, A., Ferreira-Santiago, Á., Camacho-Nieto, O., & Yáñez-Márquez, C. (2019). A machine learning approach to medical image classification: Detecting age-related macular degeneration in fundus images. *Computers & Electrical Engineering*, 75, 218–229. <https://doi.org/10.1016/j.compeleceng.2017.11.008>
20. Mookiah, M. R. K., Acharya, U. R., Koh, J. E. W., Chandran, V., Chua, C. K., Tan, J. H., ... Laude, A. (2014). Automated diagnosis of Age-related Macular Degeneration using greyscale features from digital fundus images. *Computers in Biology and Medicine*, 53, 55–64. <https://doi.org/10.1016/j.combiomed.2014.07.015>
21. Acharya, U. R., Hagiwara, Y., Koh, J. E. W., Tan, J. H., Bhandary, S. V., Rao, A. K., & Raghavendra, U. (2017). Automated screening tool for dry and wet age-related macular degeneration (ARMD) using pyramid of histogram of oriented gradients (PHOG) and nonlinear features. *Journal of Computational Science*, 20, 41–51. <https://doi.org/10.1016/j.jocs.2017.03.005>
22. Mookiah, M. R. K., Acharya, U. R., Koh, J. E. W., Chua, C. K., Tan, J. H., Chandran, V., ... Tong, L. (2014). Decision support system for age-related macular degeneration using discrete wavelet transform. *Medical & Biological Engineering & Computing*, 52(9), 781–796. <https://doi.org/10.1007/s11517-014-1180-8>
23. Hijazi, M. H. A., Coenen, F., & Zheng, Y. (2012). Data mining techniques for the screening of age-related macular degeneration. *Knowledge-Based Systems*, 29, 83–92. <https://doi.org/10.1016/j.knsys.2011.07.002>
24. Lan Du, Hongwei Liu, Zheng Bao, & Mengdao Xing. (2005). Radar HRRP target recognition based on higher order spectra. *IEEE Transactions on Signal Processing*, 53(7), 2359–2368. <https://doi.org/10.1109/TSP.2005.849161>
25. Molina, L. C., Belanche, L., & Nebot, A. (2002). Feature selection algorithms: a survey and experimental evaluation. In *2002 IEEE International Conference on Data Mining, 2002. Proceedings.* (pp. 306–313). Presented at the 2002 IEEE International Conference on Data Mining, 2002. Proceedings. <https://doi.org/10.1109/ICDM.2002.1183917>
26. Williams, B. M., Burgess, P. I., & Zheng, Y. (2019). Chapter 13 - Drusen and macular degeneration. In E. Trucco, T. MacGillivray, & Y. Xu (Eds.), *Computational Retinal Image Analysis* (pp. 245–272). Academic Press. <https://doi.org/10.1016/B978-0-08-102816-2.00013-7>
27. Kim, Y. J., & Kim, K. G. (2018). Automated Segmentation Methods of Drusen to Diagnose Age-Related Macular Degeneration Screening in Retinal Images. *Computational and Mathematical Methods in Medicine*. Research Article, Hindawi. <https://doi.org/10.1155/2018/6084798>
28. Sagar, A. V., Balasubramanian, S., & Chandrasekaran, V. (2007). Automatic Detection of Anatomical Structures in Digital Fundus Retinal Images, 4.

29. Tan, N. M., Wong, D. W. K., Liu, J., Ng, W. J., Zhang, Z., Lim, J. H., ... Wong, T. Y. (2009). Automatic detection of the macula in the retinal fundus image by detecting regions with low pixel intensity. In 2009 International Conference on Biomedical and Pharmaceutical Engineering (pp. 1–5). Presented at the 2009 International Conference on Biomedical and Pharmaceutical Engineering. <https://doi.org/10.1109/ICBPE.2009.5384075>
30. Alais, R., Dokládal, P., Erginay, A., Figliuzzi, B., & Decencièrè, E. (2020). Fast macula detection and application to retinal image quality assessment. *Biomedical Signal Processing and Control*, 55, 101567. <https://doi.org/10.1016/j.bspc.2019.101567>
31. Al-Bander, B., Al-Nuaimy, W., Williams, B. M., & Zheng, Y. (2018). Multiscale sequential convolutional neural networks for simultaneous detection of fovea and optic disc. *Biomedical Signal Processing and Control*, 40, 91–101. <https://doi.org/10.1016/j.bspc.2017.09.008>
32. Sonali, Sahu, S., Singh, A. K., Ghrrera, S. P., & Elhoseny, M. (2019). An approach for de-noising and contrast enhancement of retinal fundus image using CLAHE. *Optics & Laser Technology*, 110, 87–98. <https://doi.org/10.1016/j.optlastec.2018.06.061>
33. Mittal, D., & Kumari, K. (2015). Automated detection and segmentation of drusen in retinal fundus images. *Computers & Electrical Engineering*, 47, 82–95. <https://doi.org/10.1016/j.compeleceng.2015.08.014>
34. An Integrated System for Detection Exudates and Severity Quantification for Diabetic Macular Edema | SpringerLink. (n.d.). Retrieved November 15, 2020, from https://link.springer.com/article/10.1007%2F978-981-13-8930-6_4
35. ZhiYu Chen, Abidi, B. R., Page, D. L., & Abidi, M. A. (2006). Gray-level grouping (GLG): an automatic method for optimized image contrast Enhancement-part I: the basic method. *IEEE Transactions on Image Processing*, 15(8), 2290–2302. <https://doi.org/10.1109/TIP.2006.875204>
36. Mishra, P. K., & Kumar, A. (2020). Classification of Diabetic Retinopathy Based on Segmentation of Medical Images. In S. Bhattacharyya, D. Konar, J. Platos, C. Kar, & K. Sharma (Eds.), *Hybrid Machine Intelligence for Medical Image Analysis* (pp. 67–83). Singapore: Springer. https://doi.org/10.1007/978-981-13-8930-6_4
37. Pourreza-Shahri, R., Tavakoli, M., & Kehtarnavaz, N. (2014). Computationally efficient optic nerve head detection in retinal fundus images. *Biomedical Signal Processing and Control*, 11, 63–73. <https://doi.org/10.1016/j.bspc.2014.02.011>
38. Radon, J. (1986). On the determination of functions from their integral values along certain manifolds. *IEEE Transactions on Medical Imaging*, 5(4), 170–176. Presented at the IEEE Transactions on Medical Imaging. <https://doi.org/10.1109/TMI.1986.4307775>
39. Tavakoli, M., Mehdizadeh, A. R., Pourreza, R., Pourreza, H. R., Banaee, T., & Bahreini Toosi, M. H. (2011). Radon transform technique for linear structures detection: Application to vessel detection in fluorescein angiography fundus images. In 2011 IEEE Nuclear Science Symposium Conference Record (pp. 3051–3056). Presented at the 2011 IEEE Nuclear Science Symposium Conference Record. <https://doi.org/10.1109/NSSMIC.2011.6152552>
40. Magli, E., Olmo, G., & Presti, L. L. (1999). Pattern recognition by means of the Radon transform and the continuous wavelet transform. *Signal Processing*, 73(3), 277–289. [https://doi.org/10.1016/S0165-1684\(98\)00198-4](https://doi.org/10.1016/S0165-1684(98)00198-4)
41. Jadhav, D. V., & Holambe, R. S. (2009). Feature extraction using Radon and wavelet transforms with application to face recognition. *Neurocomputing*, 72(7), 1951–1959. <https://doi.org/10.1016/j.neucom.2008.05.001>
42. Mahfouz, A. E., & Fahmy, A. S. (2010). Fast Localization of the Optic Disc Using Projection of Image Features. *IEEE Transactions on Image Processing*, 19(12), 3285–3289. Presented at the IEEE Transactions on Image Processing. <https://doi.org/10.1109/TIP.2010.2052280>
43. Nelson, L. J., & Smith, R. A. (2019). Fibre direction and stacking sequence measurement in carbon fibre composites using Radon transforms of ultrasonic data. *Composites Part A: Applied Science and Manufacturing*, 118, 1–8. <https://doi.org/10.1016/j.compositesa.2018.12.009>
44. Automated Methods to Determine Electrospun Fiber Alignment and Diameter Using the Radon Transform. (n.d.). Retrieved September 22, 2021, from <https://www.infona.pl/resource/bwmeta1.element.springer-84777733-5375-334e-bebd-bdeb44186a78>
45. Komal, K., Bhattacharjee, N., Albrecht, D., & Srinivasan, B. (2018). Parameter Recovery Using Radon Transform. In *Proceedings of the 16th International Conference on Advances in Mobile Computing and Multimedia* (pp. 34–43). New York, NY, USA: ACM. <https://doi.org/10.1145/3282353.3282361>
46. Elloumi, Y., Akil, M., & Kehtarnavaz, N. (2018). A mobile computer aided system for optic nerve head detection. *Computer Methods and Programs in Biomedicine*, 162, 139–148. <https://doi.org/10.1016/j.cmpb.2018.05.004>
47. Jadhav, D. V., & Holambe, R. S. (2010). Rotation, illumination invariant polynomial kernel Fisher discriminant analysis using Radon and discrete cosine transforms based features for face recognition. *Pattern Recognition Letters*, 31(9), 1002–1009. <https://doi.org/10.1016/j.patrec.2009.12.026>
48. Chowdhury, A. R., Chatterjee, T., & Banerjee, S. (2019). A Random Forest classifier-based approach in the detection of abnormalities in the retina. *Medical & Biological Engineering & Computing*, 57(1), 193–203. <https://doi.org/10.1007/s11517-018-1878-0>
49. Oliveira, F. S. C., & Polito, P. S. (2018). Mesoscale eddy detection in satellite imagery of the oceans using the Radon transform. *Progress in Oceanography*, 167, 150–163. <https://doi.org/10.1016/j.pocean.2018.08.003>
50. Kantz, H., & Schreiber, T. (2004). *Nonlinear Time Series Analysis*. Cambridge University Press.

51. Pincus, S. M. (1991). Approximate entropy as a measure of system complexity. *Proceedings of the National Academy of Sciences*, 88(6), 2297–2301. <https://doi.org/10.1073/pnas.88.6.2297>
52. Richman, J. S., & Moorman, J. R. (2000). Physiological time-series analysis using approximate entropy and sample entropy. *American Journal of Physiology-Heart and Circulatory Physiology*, 278(6), H2039–H2049. <https://doi.org/10.1152/ajpheart.2000.278.6.H2039>
53. Shannon, C. E. (1948). A mathematical theory of communication. *The Bell System Technical Journal*, 27(3), 379–423. Presented at the *The Bell System Technical Journal*. <https://doi.org/10.1002/j.1538-7305.1948.tb01338.x>
54. McCamley, J. D., Denton, W., Arnold, A., Raffalt, P. C., & Yentes, J. M. (2018). On the Calculation of Sample Entropy Using Continuous and Discrete Human Gait Data. *Entropy*, 20(10), 764. <https://doi.org/10.3390/e20100764>
55. Banerjee, P., & Mondal, A. (2015, October 27). An Irregularity Measurement Based Cardiac Status Recognition Using Support Vector Machine. *Journal of Medical Engineering*. Research Article, Hindawi. <https://doi.org/10.1155/2015/327534>
56. Acharya, U. R., Fujita, H., Sudarshan, V. K., Bhat, S., & Koh, J. E. W. (2015). Application of entropies for automated diagnosis of epilepsy using EEG signals: A review. *Knowledge-Based Systems*, 88, 85–96. <https://doi.org/10.1016/j.knsys.2015.08.004>
57. Alcaraz, R., Abásolo, D., Hornero, R., & Rieta, J. J. (2010). Optimal parameters study for sample entropy-based atrial fibrillation organization analysis. *Computer Methods and Programs in Biomedicine*, 99(1), 124–132. <https://doi.org/10.1016/j.cmpb.2010.02.009>
58. Humeau-Heurtier, A. (2015). The Multiscale Entropy Algorithm and Its Variants: A Review. *Entropy*, 17(5), 3110–3123. <https://doi.org/10.3390/e17053110>
59. Song, Y., Crowcroft, J., & Zhang, J. (2012). Automatic epileptic seizure detection in EEGs based on optimized sample entropy and extreme learning machine. *Journal of Neuroscience Methods*, 210(2), 132–146. <https://doi.org/10.1016/j.jneumeth.2012.07.003>
60. Sezgin, M., & Sankur, B. (2004). Survey over image thresholding techniques and quantitative performance evaluation. *Journal of Electronic Imaging*, 13(1), 146–165. <https://doi.org/10.1117/1.1631315>
61. Liu Jianzhuang, Li Wenqing, & Tian Yupeng. (1991). Automatic thresholding of gray-level pictures using two-dimension Otsu method. In *China., 1991 International Conference on Circuits and Systems* (pp. 325–327 vol.1). Presented at the *China., 1991 International Conference on Circuits and Systems*. <https://doi.org/10.1109/CICCAS.1991.184351>
62. Lee, H., & Park, R.-H. (1990). Comments on "An optimal multiple threshold scheme for image segmentation. *IEEE Transactions on Systems, Man, and Cybernetics*, 20(3), 741–742. Presented at the *IEEE Transactions on Systems, Man, and Cybernetics*. <https://doi.org/10.1109/21.57290>
63. Brankin, E., McCullagh, P., Black, N., Patton, W., & Muldrew, A. (2006). The Optimisation of Thresholding Techniques for the Identification of Choroidal Neovascular Membranes in Exudative Age-Related Macular Degeneration. In *19th IEEE Symposium on Computer-Based Medical Systems (CBMS'06)* (pp. 430–435). Presented at the *19th IEEE Symposium on Computer-Based Medical Systems (CBMS'06)*. <https://doi.org/10.1109/CBMS.2006.157>
64. Harangi, B., & Hajdu, A. (2014). Automatic exudate detection by fusing multiple active contours and regionwise classification. *Computers in Biology and Medicine*, 54, 156–171. <https://doi.org/10.1016/j.compbiomed.2014.09.001>
65. Cao, L., & Li, H. (2020). Enhancement of blurry retinal image based on non-uniform contrast stretching and intensity transfer. *Medical & Biological Engineering & Computing*, 58(3), 483–496. <https://doi.org/10.1007/s11517-019-02106-7>
66. Shin, K. (2016). An alternative approach to measure similarity between two deterministic transient signals. *Journal of Sound and Vibration*, 371, 434–445. <https://doi.org/10.1016/j.jsv.2016.02.037>
67. Shin, K., Yang, H., Lee, S.-K., & Lee, Y.-S. (2013). Group delay based location template matching method for the identification of the impact location on a plate. *Journal of Sound and Vibration*, 332(8), 2111–2117. <https://doi.org/10.1016/j.jsv.2012.12.007>
68. Ramya, R., & Sasikala, T. (2019). An efficient Minkowski distance-based matching with Merkle hash tree authentication for biometric recognition in cloud computing. *Soft Computing*, 23(24), 13423–13431. <https://doi.org/10.1007/s00500-019-03881-z>
69. Vapnik, V. (2000). The Nature of Statistical Learning Theory. In *Statistics for Engineering and Information Science* (Vol. 8, pp. 1–15). https://doi.org/10.1007/978-1-4757-3264-1_1
70. Yu, S., Xiao, D., & Kanagasigam, Y. (2018). Machine Learning Based Automatic Neovascularization Detection on Optic Disc Region. *IEEE Journal of Biomedical and Health Informatics*, 22(3), 886–894. <https://doi.org/10.1109/JBHI.2017.2710201>
71. Ruba, T., & Ramalakshmi, K. (2015). Identification and segmentation of exudates using SVM classifier. In *2015 International Conference on Innovations in Information, Embedded and Communication Systems (ICIIECS)* (pp. 1–6). Presented at the *2015 International Conference on Innovations in Information, Embedded and Communication Systems (ICIIECS)*. <https://doi.org/10.1109/ICIIECS.2015.7193219>
72. Zheng, Y., Hijazi, M. H. A., & Coenen, F. (2012). Automated “disease/no disease” grading of age-related macular degeneration by an image mining approach. *Investigative Ophthalmology & Visual Science*, 53(13), 8310–8318. <https://doi.org/10.1167/iovs.12-9576>
73. Ayinala, M., & Parhi, K. K. (2012). Low complexity algorithm for seizure prediction using Adaboost. In *2012 Annual International Conference of the IEEE Engineering in Medicine and Biology Society* (pp.

- 1061–1064). Presented at the 2012 Annual International Conference of the IEEE Engineering in Medicine and Biology Society. <https://doi.org/10.1109/EMBC.2012.6346117>
74. (15) SVM-based Real-Time Hyperspectral Image Classifier on a Manycore Architecture | Request PDF. (n.d.). ResearchGate. Retrieved February 6, 2020, from https://www.researchgate.net/publication/319248130_SVM-based_Real-Time_Hyperspectral_Image_Classifier_on_a_Manycore_Architecture
 75. Usage Models. (n.d.). Retrieved September 14, 2020, from https://docs.nvidia.com/tegra/Content/OpenCV_Usage_Models.html
 76. The STARE Project. (n.d.). Retrieved October 19, 2020, from <https://cecas.clemson.edu/~ahoover/stare/>
 77. REFUGE - Grand Challenge. (n.d.). grand-challenge.org. Retrieved November 9, 2021, from <https://refuge.grand-challenge.org/>
 78. Pachade, S., Porwal, P., Thulkar, D., Kokare, M., Deshmukh, G., Sahasrabudhe, V., ... Mériaudeau, F. (2021). Retinal Fundus Multi-Disease Image Dataset (RFMiD): A Dataset for Multi-Disease Detection Research. *Data*, 6(2), 14. <https://doi.org/10.3390/data6020014>
 79. OpenCV. (n.d.). Retrieved December 24, 2019, from <https://opencv.org/>
 80. ODBOT: Outlier detection-based oversampling technique for imbalanced datasets learning | SpringerLink. (n.d.). Retrieved December 2, 2021, from <https://link.springer.com/article/10.1007/s00521-021-06198-x>
 81. Chawla, N. V., Bowyer, K. W., Hall, L. O., & Kegelmeyer, W. P. (2002). SMOTE: Synthetic Minority Over-sampling Technique. *Journal of Artificial Intelligence Research*, 16, 321–357. <https://doi.org/10.1613/jair.953>
 82. Labonne, M., Olivereau, A., Polvé, B., & Zeghlache, D. (2019). A Cascade-structured Meta-Specialists Approach for Neural Network-based Intrusion Detection. In 2019 16th IEEE Annual Consumer Communications Networking Conference (CCNC) (pp. 1–6). Presented at the 2019 16th IEEE Annual Consumer Communications Networking Conference (CCNC). <https://doi.org/10.1109/CCNC.2019.8651856>
 83. Han, H., Wang, W.-Y., & Mao, B.-H. (2005). Borderline-SMOTE: A New Over-Sampling Method in Imbalanced Data Sets Learning. In D.-S. Huang, X.-P. Zhang, & G.-B. Huang (Eds.), *Advances in Intelligent Computing* (pp. 878–887). Berlin, Heidelberg: Springer. https://doi.org/10.1007/11538059_91
 84. Wang, K.-J., Adrian, A. M., Chen, K.-H., & Wang, K.-M. (2015). A hybrid classifier combining Borderline-SMOTE with AIRS algorithm for estimating brain metastasis from lung cancer: A case study in Taiwan. *Computer Methods and Programs in Biomedicine*, 119(2), 63–76. <https://doi.org/10.1016/j.cmpb.2015.03.003>
 85. Glaucoma disease diagnosis with an artificial algae-based deep learning algorithm | SpringerLink. (n.d.). Retrieved February 19, 2022, from <https://link.springer.com/article/10.1007/s11517-022-02510-6>
 86. Friedman, M. (1940). A Comparison of Alternative Tests of Significance for the Problem of m Rankings. *The Annals of Mathematical Statistics*, 11(1), 86–92. Retrieved from <https://www.jstor.org/stable/2235971>
 87. Khalid, S., Akram, M. U., Shehryar, T., Ahmed, W., Sadiq, M., Manzoor, M., & Nosheen, N. (n.d.). Automated diagnosis system for age-related macular degeneration using hybrid features set from fundus images. *International Journal of Imaging Systems and Technology*, n/a(n/a). <https://doi.org/10.1002/ima.22456>
 88. Rajinikanth, V., Sivakumar, R., Hemanth, D. J., Kadry, S., Mohanty, J. R., Arunmozhi, S., ... Nhu, N. G. (2021). Automated classification of retinal images into AMD/non-AMD Class—a study using multi-threshold and Gaussian-filter enhanced images. *Evolutionary Intelligence*, 14(2), 1163–1171. <https://doi.org/10.1007/s12065-021-00581-2>
 89. Heyang, Y. Q. W., & Heyang WANG, Q. Y. (n.d.). A screening and recognition method for multiple diseases of the retina based on deep convolutional integrated networks. *Journal of Intelligent Science and Technology*, 3(3), 259–267. <https://doi.org/10.11959/j.issn.2096-6652.202127>



Sofien BENSAYADIA is a joint Ph.D student at the University of Gustave Eiffel Marne-la-Vallée (France) and the University of SOUSSE (Tunisia). he got a research master degree in Systèmes Pervasifs Intelligents (MR-SPI) in 2018. Her current research areas deal with His research focuses primarily on the image processing algorithms, computer vision, real-time image processing and intelligence artificiel.



Yaroub Elloumi received his PhD in co-supervision with the University of Paris-Est Marne-la-Vallee (France) and the University of Sfax (Tunisia) in 2013. He received his MS in Real-Time Systems from the University of Sousse (Tunisia) in, 2008. He currently teaches and does research with the position of Assistant Professor in Computer Sciences. He is a member of both Gaspard Monge Computer Science Laboratory (LIGM CNRS UMR 8049) and Medical Technology and Image Processing Laboratory (LabTIM LR12ES06). His research interests are computer vision, parallel computing and real-time image processing.



Rostom Kachouri received his Engineers and Master degrees from the National Engineering School of Sfax (ENIS) in 2003 and 2004, respectively. In 2010, he received his Ph.D. in Image and Signal Processing from the University of Evry Val d'Essonne. From 2005 to 2010, Dr. Kachouri was an Assistant Professor at the National Engineering School of Sfax (ENIS) and then at the University of Evry Val-d'Essonne. From 2010 to 2012, he held a postdoctoral position at ESIEE Paris as part of a project with the high technology group SAGEMCOM. Dr. Kachouri is currently associate professor at ESIEE Paris. He is a member of the Institut GaspardMonge, unite´ mixte de recherche CNRS-UMLPE-ESIEE, UMR 8049. His research works concern mainly the Signal and Image processing (Pattern Recognition, Segmentation, OCR systems) and the Algorithm-Architecture Matching (GPU, FPGA).



Mohamed Akil received his PhD degree from Montpellier University (France) in 1981 and his doctorat d'etat (DSc) from the Pierre et Marie curie University (UPMC, Paris, France) in 1985. Since September 1985, he has been with ESIEE Paris that is the CCIR's (Chambre de commerce et d'industrie de region Paris Ilede-France) center for scientific and engineering education and research. He is currently a Professor in the Computer Science Department, ESIEE Paris. He is a member of the Laboratoire d'Informatique Gaspard Monge, Université Paris-Est Marne-la-Valée (UMR 8049, unité mixte de recherche CNRS), a joint research laboratory between Université Paris-Est Marne-la-Vallée (UPEM), ESIEE Paris and École des Ponts ParisTech (ENPC). He is member of the program committee of the SPIE-Real-Time Image and Video Processing conference (RTIVP). He is member of the Editorial Board of the Journal of Real-Time Processing (JRTIP). His research interests include dedicated and parallel architectures for image processing, image compression and virtual reality. His main research topics are parallel and dedicated architectures for real time image processing, reconfigurable architectures and FPGA, high-level design methodology for multiFPGA, mixed architecture (DSP/FPGA) and Systems on Chip (SoC). He has published more than 160 research papers in the above areas.



Asma Ben Abdallah was born in Tunisia on March 20, 1972. She hold her Ph.D. in computer science from the National Institute of Computer Science (ENSI) in Tunisia in 2007. Since 2004, she was an Assistant Professor on informatics at the High Institute of Application Science and Technology in Sousse. Since 2008, she was an Assistant Professor on informatics at the Higher Institute of Informatics and Mathematics of Monastir (ISIMM), in Tunisia and Since 2018, she is Professor on informatics at the same institution (ISIMM). On research, she works in the Laboratory of Technology and Medical Imaging (LTIM), at the Faculty of Medicine of Monastir, University of Monastir, Tunisia. Her current interests include computer vision-imaging.

Mohamed Hedi Bedoui was born in 1965 in Teboulba, Tunisia. He is an engineer in electronics (ENIS-University of Sfax in 1988); He obtained his Ph.D. Biomedical Engineer at the University



of Lille, France, in 1993. He is Professor in Biophysics at the Faculty of Medicine of Monastir, Director of the laboratory LTIM (Technologies and Medical Imaging) -LR12ES06 and President of the Society Tunisian Association for the Promotion of Applied Research ATUPRA. His current interests include modeling and processing medical data from the sensor to optimizing the implementation of embedded systems.